The mechanical behaviour of a slip joint for an offshore wind turbine
First monitoring and modelling results

Mojto, Maroš; Cabboi, Alessandro

DOI
10.1016/j.tws.2023.111482

Publication date
2023

Document Version
Final published version

Published in
Thin-Walled Structures

Thin–Walled Structures 196 (2024) 111482

Contents lists available at ScienceDirect

Thin-Walled Structures

journal homepage: www.elsevier.com/locate/tws

Full length article

The mechanical behaviour of a slip joint for an offshore wind turbine: First monitoring and modelling results

Maroš Mojto [a], Alessandro Cabboi [b,*]

[a] Faculty of Civil Engineering, Slovak University of Technology in Bratislava, Radlinského 2766/11, 810 05 Bratislava, Slovakia
[b] Faculty of Civil Engineering and Geosciences, Delft University of Technology, Stevinweg 1, 2628CN Delft, Netherlands

ARTICLE INFO

Keywords:
Wind energy
Steel connection
Contact mechanics
Strain monitoring

ABSTRACT

This study aims at shedding light on the mechanical behaviour of a prototype monopile–wind turbine tower connection, constituted by a slip joint. Selected examples of data set recorded during a long term monitoring campaign are illustrated and discussed. The data set encompass axial and hoop stresses measured over the slip joint area, relative displacements of the slip joint with respect to the monopile and acceleration levels recorded above the slip joint. In parallel, an ideal and simplified Finite Element model (FEM) of the slip joint is developed, in order to interpret the observed experimental data. Experiments first highlight the relevance of modelling the manufacturing imperfections of the overlapping steel sections. Subsequently, both experiments and FEM show that states of prestress need to be accounted for. Such prestress states first originate from the installation process, and subsequently from further loading events, triggering settlements of the slip joint. Finally, experiments and FEM showcase the force transfer mechanisms from the upper part to the lower part of the slip joint.

1. Introduction

1.1. Brief introduction to the slip joint technology

The slip joint technology represents an alternative connection based on the overlap between two conical pipes with a circular or also polygonal cross-section. The reliability of the connection depends on the sound transfer of forces from the upper cone to the lower cone, thanks to the chosen geometrical overlap and the friction force generated between the surfaces in contact. Since neither welds, bolts nor grouts are needed to ensure the connection, this results in a significant reduction of the installation time. The concept of using a slip joint is not new per se and is commonly used in civil engineering constructions, such as for masts, columns, towers, or poles, as an alternative to the traditional solution of using flanged joints, welds or grout. This paper focuses on the assessment of the slip joint's mechanical behaviour for a wind turbine tower, that would be commonly installed on support structures, such as monopiles or jacket structures.

Within the wind energy community, the need to search for alternative and reliable connection techniques became pressing towards the end of 2009. Around 600 European wind tower installations, assembled through a grouted connection, started to exhibit a failure mechanism, characterized by cracks and a downward slip. In 2010, the offshore wind developers recognized that one of the key design and retrofitting challenges they had to face was related to the issue of dissolved grouting, and this was reason enough to set up a Joint Industry Project, to seek possible solutions for the grouting problem [1–3]. Concurrently, this also triggered new research studies aiming to pin down the failure mechanisms of the grouted connection [4–10], and at the same time proposing new design solutions [3,11–17]. A further option that could be used in substitution to the grouted connection consists of bolted flanges. However, in order to ensure the desired life-time for such type of connections, extra costs may be needed for the installation [18] and maintenance phase [19,20]. A recent example of the consequences caused by lack of maintenance for bolt connections, is given by the collapse of a wind turbine installed in Lemnhult (Sweden): in 2015 the structure collapsed due to the loss of bolt tightness [21]. Of course, improvements to traditional bolt connections for tubular wind turbine towers are currently proposed, see the C1 Wedge Connection for example [22], reducing the risk of the bolt preload loss, and therefore minimizing maintenance costs.

As mentioned above, an alternative solution to the use of grouts or bolts, consists of using a slip joint, for which a first feasibility study for offshore applications was conducted in 2003 [23]. In 2018, a couple of joint projects (SJOR and SJOQ project, Slip Joint Offshore Research and Slip Joint Offshore Qualification, respectively) between Delft University of Technology (TUD) and various companies such

* Corresponding author.
E-mail address: A.Cabboi@tudelft.nl (A. Cabboi).

https://doi.org/10.1016/j.tws.2023.111482
Received 8 September 2023; Received in revised form 25 October 2023; Accepted 10 December 2023
Available online 12 December 2023

as DOT, TNO, VanOord, and SIF, were aimed to promote and test a prototype slip joint for offshore applications. The reader may refer to the following webpage [24] for a more complete summary and for few video clips and reports on the final outcomes of the project. As a result, in September 2018, the tower of a 500 kW hydraulic DOT500 wind turbine was mounted on a monopile through a slip joint (see Section 2 for a more detailed description). The focus of this study refers to understand the observed structural behaviour of the installed slip joint, that was monitored from October 2018 until its decommissioning that occurred in two steps between May and August 2019. Since the monitoring is part of a joint industrial–academic project, note that the results shown in this report only includes the data available for TU Delft. As a follow-up of the SJOR and SJOQ projects, it is worth mentioning the installation of the world's first full-size submerged slip joint connection, in April 2020, at the Borssele Site V offshore wind farm [25].

1.2. Current challenges for the slip joint technology and research objective

Although the slip joint technology is not new, its mechanical interface behaviour has not been fully understood so far. Currently, only few technical reports are available [26], with scarce recommendations on how to design the connection. As an example, the only requirements requested by European Standards [27] is to meet the minimum overlap length between the two cones, defined as 1.5 times the diameter of the cross-section. Within the context of saving and reducing material-related costs, the question arises whether such a requirement is too conservative. Indications are also not provided with reference to the expected behaviour of axial and hoop stresses within the overlapped contact area, during specific loading scenarios (in short- and long-term), and in relation to the influence of contact overlap, conicity or installation imperfections on the overall behaviour of the connection. In the absence of such recommendations, designers may be forced to consider contact scenarios by assuming extreme contact discontinuity or non-uniformity between the upper and lower part of the connection, in order to generate an envelope of the allowable operational condition of the slip joint. However, the above-mentioned design approach is still too rudimentary, highlighting large margins of improvements.

A few studies have been performed by the Department of Steel and Timber Structure of the SUT in Bratislava concerning the mechanical behaviour of slip joints, with the global aim of verifying the structural capacity of slip joints and possibly reducing the overlapping length. Specifically, the results of field tests [28,29] and laboratory tests [30] for slip joints meant for electrical transmission towers were reported. The tested slip joints were characterized by circular and polygonal cross-sections [29,30]. In both studies, analytical and numerical models were developed to simulate and explain the experimental behaviour. The results indicated that geometric imperfections between the overlapped surfaces are a key factor to correctly understand the experimental outcome. Follow-up studies [31,32] included such contact imperfections in the numerical Finite Element (FE) model, leading to a partial validation of the FE model. The relevance of modelling the surface imperfections was also pointed out in a more recent study concerning the installation of an offshore slip joint [25].

Besides the manufacturing imperfections, the most practical challenge within the offshore industry, concerns the installation and decommissioning of the slip joint. This aspect was extensively discussed in previous works [33,34], and in which a solution was illustrated and tested based on exploiting a deliberate applied vibration on the slip joint. A tailored oscillatory force applied during the installation and decommissioning phase, enforces settlements of the slip joint and also reduce the friction, for the two phases respectively. However, more tests are still needed to corroborate the working principle, and a reliable modelling strategy able to predict ahead the induced settlements and the release of friction prestress is still missing. A further challenge connects to what has been described before, and refers to the lack of (experimental) knowledge concerning the interface mechanics occurring within the slip joint. Since the stress flow within the slip joint depends on the contact configuration and the frictional force between the two overlapped conical parts, the desired aim would be to reliably predict possible changes of the contact configuration and the friction force during the designed life-time of the slip joint with respect to environmental and operational loading conditions of the wind turbine.

To start shedding light on this challenge, this study aims at interpreting the results obtained by the measuring campaign of the 500 kW hydraulic DOT500 wind turbine, connected to its monopile by means of a slip joint. Firstly, we present a general overview of the evolution of the main measured quantities available, such as axial stress, hoop stress, differential displacements and acceleration. The different sets of data available, refer to specific events (i.e. deliberate blade rotation, wind and wave loads), capturing different stress states caused by specific operational and environmental conditions. Specifically, in the first part of the paper, it will be shown how the axial stress pattern is able to reflect the soundness of the force transfer from the upper to the lower part, how the hoop stresses can provide an indication of the extension of the contact area at the bottom and upper part of the slip joint, how the settlement of the slip joint evolves in time, and the stable behaviour of the first two bending modes of the investigated structure during specific operational conditions. Additionally, results will be shown with reference to the installation process of the upper tower, and the corresponding generated prestress present at upcoming loading events. In the second part, a FE model representative of the slip joint is described. At this stage, and considering the complexity of the measured data available, the aim of the FE model is to qualitatively interpret the observed experimental results, with reference to the stress transfer mechanism from the upper part to the lower part, and the structural behaviour of the slip joint under a vertical force and a bending moment. Preliminary results from the FE model also allows to explain some unexpected hoop stress patterns, highlighting the need to account for the loading history to accurately capture the presence of residual stresses.

This paper is organized as follows. In Section 2, the case study is introduced and the monitoring campaign is described. Section 3 provides the first insights into the experimental data and attempts to explain and highlight some unexpected phenomena that were observed. In Section 4 and Section 5, the experimental data is qualitatively explained by means of simulations performed by the developed FE model. Finally, we summarize this study's main conclusions, and provide a discussion on the current state of the art concerning the slip joint and possible future research lines.

2. Case study and monitoring campaign

2.1. Description of the slip joint and the wind turbine tower

The case study presented in this work is a prototype 500 kW wind turbine, that was assembled at the Princess Amalia Wind Farm, located 23 km from the Dutch coast at the North Sea. The lower part of the wind turbine tower was directly mounted on top of a monopile (MP) by means of a slip joint. A general view of the case study is shown in Fig. 1a, the major dimensions of the overall structure and in particular of the slip joint are illustrated in Fig. 1b.

The total height is about 92 m and the total dead-weight acting on the slip joint was around 86.5 ton. The wall thickness of the curved steel plates forming the monopile decreases with increasing height starting from the seabed, from 65 mm to 40 mm at the overlapping region forming the slip joint (see grey shading in Fig. 1b). The final extension of such overlap after installation is about 5.19 m (note that the designed overlap was 5.20 m). The wall thickness of the external cone overlapping with the monopile is 15 mm and the cone angle is 88.26° with reference to the horizontal plane (see Fig. 1b). Note that the existing monopile is also characterized by a slight inclination with

(a) Picture of the DOT wind turbine, see also [24].

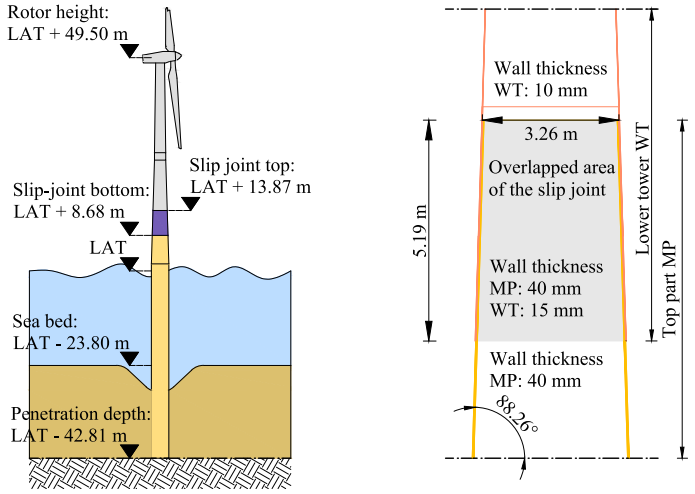

(b) Schematic layout of the entire structure and the slip joint.

Fig. 1. General view and schematics of the wind turbine and the slip joint. The shaded grey area in Fig. 1(b) defines the overlapped region covered by the slip joint. MP stands for monopile, while WT refers to the wind turbine tower. (For interpretation of the references to colour in this figure legend, the reader is referred to the web version of this article.)

respect to the vertical direction of 0.4°. For further details about the few design criteria adopted to design the slip joint, the reader may refer to a previous work [34]. However, as discussed in the introduction, no specific DNV (Det Norske Veritas) guidelines are available to design such connections for offshore applications, and monitoring strategies should be developed to track the mechanical behaviour of the slip joint within the offshore environment over time.

2.2. Monitoring campaign

A monitoring campaign started in October 2018, running for a total of 8 months until May 2019. The monitoring activity was part of the SJOQ project [35], a joint effort between industry and academia to monitor the mechanical behaviour of the slip joint. A schematic overview of the sensors' layout used for the monitoring campaign is shown in Fig. 2. The adopted sensors allowed to partially reconstruct the local stress distribution characterizing the slip joint behaviour under different operational and environmental conditions. The sensing setup consisted of a large array of optical fibre sensors measuring the axial strain, mounted on the outer wall of the wind turbine tower (WT) and on the inner side of the monopile. The blue dashed lines in Fig. 2 indicate the location of such sensors along the height of the slip joint, for a total of 7 instrumented cross-sections, while their distribution over the cross-section is shown by the blue cross markers displayed on symbolic circles on the right side of Fig. 2. Such circles mimic the top view of the corresponding instrumented cross sections. Note though that the diameter of such circles are not proportional with the actual varying slip joint diameter. The green dashed lines and circle markers refer to the optical fibres measuring the tangential circumferential (hoop) strains, which were mounted on two circumferential sections on the outer part of the WT. For the latter, each cross-section was instrumented with 36 sensors. The relative displacement between the WT and the MP is monitored using LVDTs, linear displacement sensors, which location is indicated by the brown dashed line and cross markers in Fig. 2. The cyan circles in Fig. 2 refer to the location where temperature data has been collected. In addition, one tri-axial accelerometer was also mounted in section S1.

Due to agreements between the industrial and university partners involved within the project, this study only makes a limited use of the overall data recorded during the 8 months monitoring campaign. The analysed data includes a series of selected events during which either a significant environmental load (i.e. winter storms and wave slamming events) or a deliberate operational load (e.g. multiple emergency-stop procedures of the turbine) was induced. Each recorded event has a duration of approximately 30 min. The focus during these events is upon the axial and circumferential strains, and measured displacements of the slip joint. Considering the large amount of data, these events aims at providing a first insight of the most meaningful data available. It suffices to say that during the monitoring period the measured relative displacements, and therefore settlements of the slip joints, showed a tendency to stabilize over time. In addition, after each significant loading event, hoop and axial strains stayed below the yield limit for steel.

3. Interpretation of monitoring results

This chapter provides a summary of the collected monitoring results, limited to the shareable data with TU Delft. To keep the paper within a reasonable length, priority has been given to the most representative results concerning the mechanical behaviour of the slip joint. Few sensors were also subject to malfunctioning, hence outlier behaviour can be spotted. It is important to highlight that the assembled wind turbine was a prototype one, and only operating on demand, according to the experimental needs.

In general, hoop and axial strains were measured during the installation process. Whereas throughout the entire time-window of the monitoring campaign, hoop and axial strains, relative displacements and acceleration levels were measured. Data was continuously recorded, but the available (shareable) data set refer to 14 spread "events" that occurred during the monitoring campaign. The "event" is formed by a data set that has a duration of 30 min, and events are related to specific operational conditions such as a deliberate rotation of the blades, or particularly harsh environmental conditions in terms of strong wind gusts and rough sea conditions. The start of each event data set was provided with nulled values, in order to highlight the relative variation of the measured quantities with reference to the specific event that occurred during the selected time-window of 30 min.

Only few events are selected for this paper, in order to highlight the most significant mechanical behaviour of the slip joint useful for the development of the numerical model, described in Section 4. A typical data set of a selected event is illustrated in Fig. 3. For the specific chosen example, axial stresses are reported, which refer to cross section S2 (see Fig. 2), and the rotation per minute of the blades (RPM) is displayed, since the wind turbine was switched on for that specific

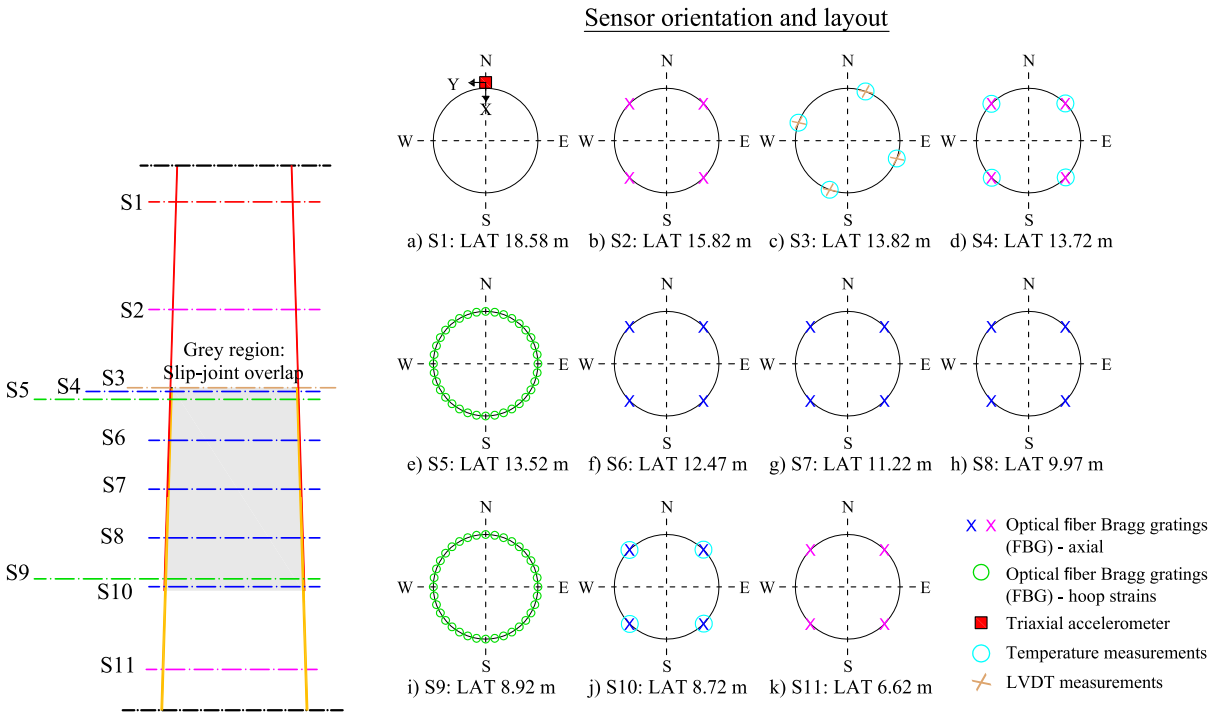

Fig. 2. Sensor layout over the slip joint. The sensors marked by the blue line are installed on the outside shell of the upper tower and on the inside shell of the monopile (two sensors at the same level (outside-inside); the sensors marked by the pink line (S2) are only on the outer shell of the upper tower and (S11) on the inside shell of the monopile. The green lines and markers refer to the sensors measuring the circumferential strain, while the brown and cyan symbols refer to the LVDT sensors and thermocouples installed in the slip joint. (For interpretation of the references to colour in this figure legend, the reader is referred to the web version of this article.)

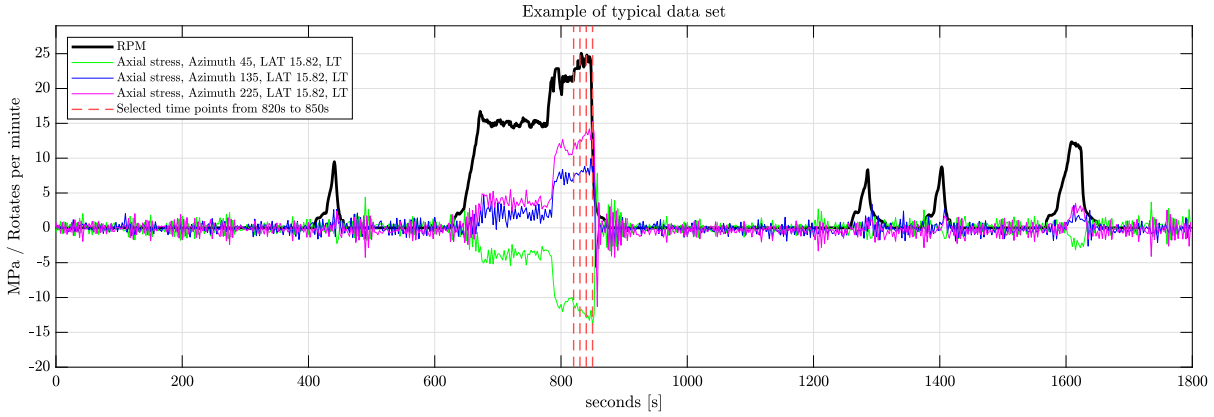

Fig. 3. Example of a 30 min event, measured on the 04/10/2018, starting at 17:34. Axial stress and RPM of the blades are reported. This event is labelled as n. 01. LT stands for the lower tower of the wind turbine. (For interpretation of the references to colour in this figure legend, the reader is referred to the web version of this article.)

event. The variation of the axial stress highlights an increase as soon the blades start operating (around 600 s). For each event, peaks can be detected in terms of either axial stresses, hoop stresses, displacements and accelerations. Throughout the paper, the focus will be especially on such peaks, captured by multiple time points (red lines in Fig. 3).

At first, the long term behaviour of the slip joint in terms of hoop stresses and displacement is presented. A qualitative comparison between the observed hoop stress and simplified analytical expressions to estimate the hoop stress for a slip joints is discussed. Subsequently, data related to specific events and corresponding peaks are presented. In particular with reference to events in which blades were rotating, both at the beginning and towards the end of the monitoring campaign, and to events which were mainly characterized by wind and wave loads. To conclude this Section, the relevance of the prestress is discussed with reference to the measured hoop stress, which exhibit some sort of memory effect.

3.1. Long-term behaviour of selected measured quantities

3.1.1. Hoop stress variation during the installation process and at the end of the monitoring campaign

The installation process of the lower tower onto the monopile was carried out on the 30/09/2018. The process of overlapping started approximately at 7:00 AM. The settlement mechanism during the installation process mainly relied on the self weight of the lower tower. As mentioned earlier, hoop stresses were recorded during the installation process and their variation is captured in Fig. 4 with reference to the cross sections S9 (LAT09), Fig. 4a, and S5 (LAT14), Fig. 4b, starting at 07:45 AM. Both figures show the evolution of the hoop stress for the subsequent 16 h.

It is interesting to note that right after an initial overlap is achieved (the measured overlap was 5.19 m, while the target overlap was

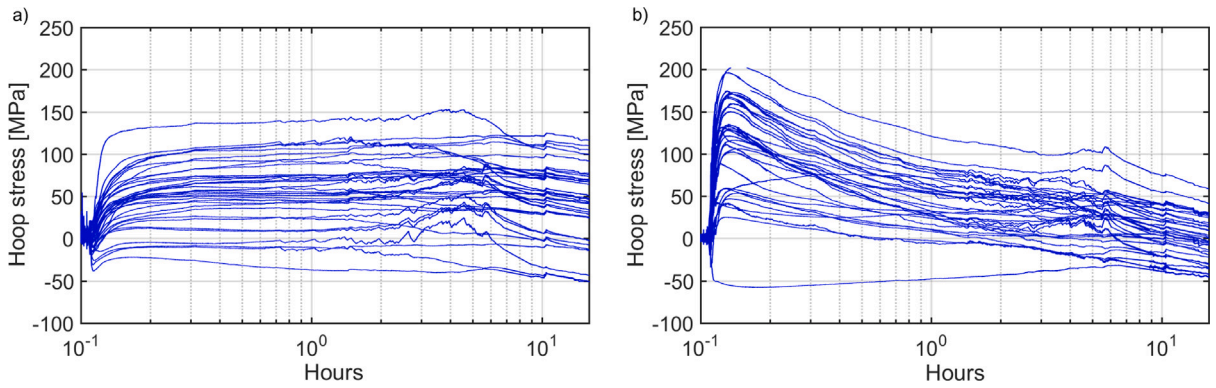

Fig. 4. Variation of the hoop stresses during the installation process, for the instrumented cross section at (a) S9 (LAT09) and (b) S5 (LAT14). The time zero in each plot corresponds to 7.45 AM, recorded the 30/09/2018.

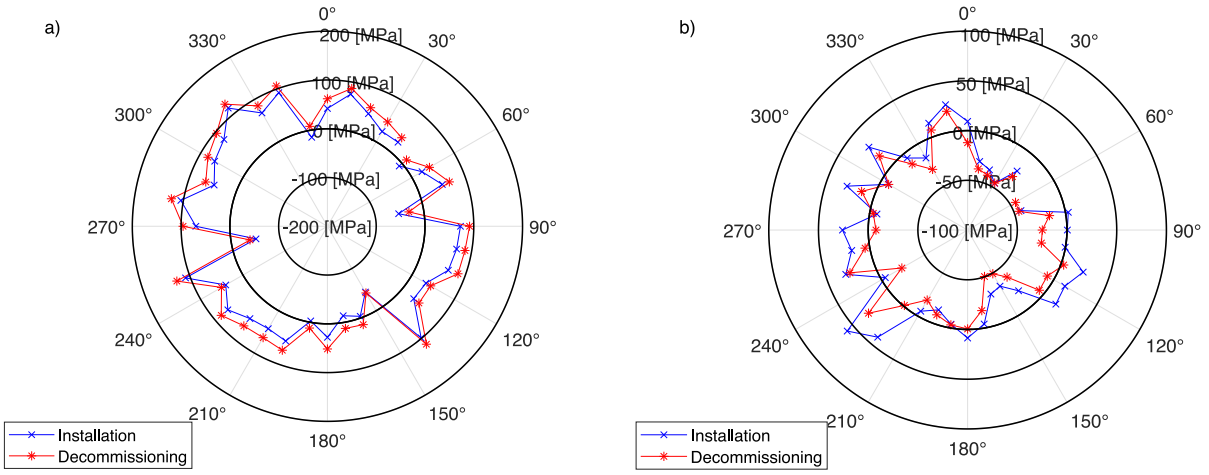

Fig. 5. Variation of the hoop stresses between the installation process and the last days of monitoring, for the instrumented cross section at (a) S9 (LAT09) and (b) S5 (LAT14). The time instant for the installation data (blue lines) is 0:00 recorded the 1/10/2018, while for the last days of monitoring is 0:00 recorded the 22/05/2019. (For interpretation of the references to colour in this figure legend, the reader is referred to the web version of this article.)

5.20 m), several sensors located at the cross section S5, Fig. 4b, captured significantly higher circumferential stress levels, corresponding to hoop stresses between 100–200 MPa, compared to the hoop stresses observed at cross section S9, Fig. 4a, that were gradually increasing with a certain time delay. The difference in the hoop stress distribution between the top and bottom cross section seems to indicate that the initial load transfer between the two overlapping cones occurs at the top part of the slip joint. As time passes, the slip joint keeps settling and displacing downwards, therefore increasing the effective contact area. After 16 h, Fig. 4 shows that the hoop stresses reach steady values at both cross sections. On that note, it is worth highlighting that the hoop stresses for cross section S5 distribute themselves between −50 and 50 MPa, while for cross section S9 the range is somewhat higher, specifically between −50 and 120 MPa.

Fig. 5 shows a comparison between the hoop stress values recorded after 16 h from the time of first overlap and the values measured 2 days before the removal of the sensors, that occurred the 24th of May 2019. Besides these two time instants that show similar hoop stresses, it is worth remarking that the same trend can be observed during the whole monitoring campaign, indicating a fairly steady behaviour of the hoop stress distribution due to the dead loads between October 2018 and May 2019. Note that this gives origin to a first state of prestress that persists in the slip joint during the whole monitoring period. A common feature that can be observed in both cross sections is the transition between positive (tension) and negative (compression) hoop stresses that occurs along the circumference. This pattern may be caused by alternating contact and non-contact spots along the circumference due to manufacture imperfections of the assembled/welded plates that form the cones of the slip joint. The main difference of the hoop stress distribution between the two cross sections (besides the amplitudes), consists in the predominant presence of a tensile hoop stress state at the bottom cross section, implying a more uniform contact area distribution at cross section S9, see Fig. 5a. With reference to cross section S5, see Fig. 5b, a larger segment of the circumference (between 0° and 70°) is subject to a compressive hoop stress state, possibly implying a larger contact gap at the top part of the slip joint. The latter could be either caused by the above-mentioned manufacturing imperfections and/or by the presence of bending moments caused by the eccentricity due to the blades and to the inherent inclination of the existing monopile. The inclination of the monopile with respect to the vertical direction is of 0.4°, tilting over the 25°–205° direction.

To assess whether the observed hoop stresses could be predicted by a simplified analytical model based on structural mechanics principle, the formulas derived in [23] and also discussed in [26,36] are used. The hoop stress distribution caused by the installation process may result from the superposition of two dead loads: the vertical self-weight of the upper tower and the bending moment caused by the presence of the above-mentioned eccentricities. The resulting effect is expressed as follows

$$\sigma_{hoop} = \sigma_{hoop,A} + \sigma_{hoop,B} = \frac{F_z}{2t\gamma h\pi \tan(\theta + \mu_s)} + \frac{3M_{y,ecc}}{th^2} \quad \left[\frac{\mathrm{N}}{\mathrm{m}^2}\right] \tag{1}$$

where $\sigma_{hoop,A}$ and $\sigma_{hoop,B}$ stand for the hoop stress due to the axial load (F_z) and the bending moment ($M_{y,ecc}$), respectively. Parameters t, γ,

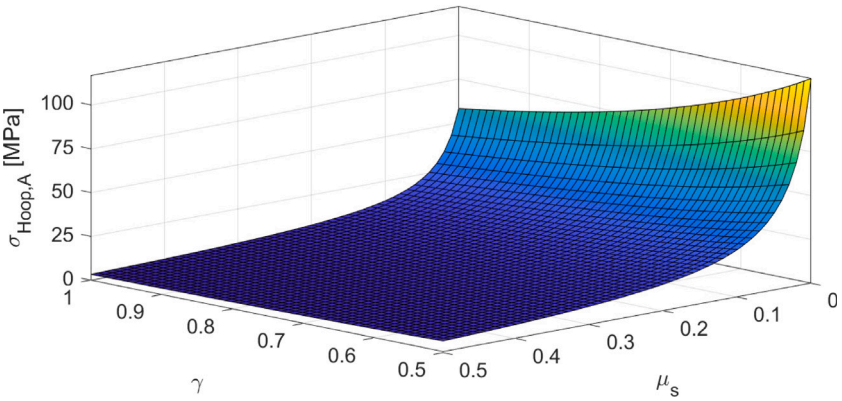

Fig. 6. Variation of the hoop stress due to an axial load, for a varying contact area and coefficient of static friction. The varying contact area is qualitatively simulated through a weighting factor γ, for which 1 represents a perfect fit between the overlapping cones and 0.5 qualitatively indicates a reduced contact area of 50%.

h, θ and μ_s refer to the wall thickness, a weighting parameter for the actual overlap ranging between 0.5 and 1, the overlap height of the slip joint, the cone angle with respect to the longitudinal axis and the static coefficient of friction between the two overlapping cones. Eq. (1) relies on stringent assumptions such as a perfect fit between the two overlapping cones which leads to a uniform contact area, and a linearly increasing distribution of the contact stress due to the bending moment, along the slip joint's height. Imperfections and the actual overlap length of the slip joint may prevent the compliance of such assumptions. For instance, the actual contact area may be formed by localized parts in contact, and the corresponding contact stress variation may not follow a linear relationship with the height of the slip joint. On such regard, the findings in [32] and the recommendations provided in [25], highlight that to achieve an accurate model, the manufacture imperfections cannot be neglected. On top of that, as discussed in [34], the behaviour of the friction force between the two overlapping (coated) steel cones is subject to uncertainties and most likely tends to vary over time due to the wear process of the coating caused by slipping. The possible variation of the hoop stress range due to the vertical dead load F_z (hence, excluding the bending moment contribution) is qualitatively shown in Fig. 6, where the varying parameters were γ (0.5–1), representative of the unknown contact area, and the coefficient of friction (0–0.5). Low values of the static friction coefficient can be justified due the presence of the coating on the steel surface, which may significantly reduce the resistance to motion. The vertical dead load is assumed to be 870 kN and the cone angle θ equal to 1.74°. Since the full dead load of the wind turbine tower is considered, the results shown in Fig. 6 should be compared with the measured hoop stresses at section S9 (LAT09).

The most noticeable behaviour in Fig. 6 is that for increasing values of the coefficient of static friction, the hoop stress in the wind turbine tower reduces, due to the increasing stress transfer between the wind turbine tower and the monopile. It can also be noted that in case of a perfect fit between the two overlapping cones (γ=1), and for a varying coefficient of static friction between 0 and 0.5, the hoop stress can vary between 3–58 MPa, while most of the values recorded at section S9 fluctuate between 50–100 MPa. To approach the measured values, one may assume a reduced contact area due to imperfections. As shown in Fig. 6, a qualitative reduction of the contact area by 50%, can lead to an increased range of hoop stresses between 6–116 MPa, for varying values of μ_s. If the additional hoop stresses, $\sigma_{hoop,B}$, due to the bending moments are also added, the increase of the actual hoop stress is rather moderate since $\sigma_{hoop,B}$ tends to approximately vary between 1–8 MPa, taking into account the uncertainty due to the actual eccentricity (the orientation of the nacelle-blade assembly can vary) and the effective contact area. With the reference to the latter note, it is worth highlighting that the value 3 at the denominator in Eq. (1) carries the uncertainty of the effective contact length between the upper and lower part of the slip joint. Overall, the comparison between Eq. (1) and the measurements, clearly show that a perfect fit between the two cones would only explain the recorded hoop stresses if no friction force would be present. If friction is taking into account, the hoop stresses tend to decrease and only by accounting for eventual imperfections (and for low coefficient of static friction, <0.1), the estimated values of the hoop stress tend to approach the recorded ones.

3.1.2. Variation of the LVDT displacements

During the installation of the slip joint, the achieved overlap was 5.19 m, while the target overlap based on the geometrical design of the slip joint was 5.20 m. Subsequently to the installation, settlements of the slip joint occurred. Such settlements are highlighted in Fig. 7a, that illustrates the long-term trend of the estimated mean values for each event data set of the displacement for all LVDT sensors. It can be noted that four days after the installation, the measured displacement is about 8 mm. For the subsequent four months, a drop of about 6 mm has been recorded (14 mm in total). Between day 120 and 180, the displacements slowly stabilize in time. It is worth noting that the installation has been performed without the assistance of vibro-shakers, as suggested in [33], which can facilitate and enforce the initial settlement of the slip joint, eventually minimizing significant follow-up settlements. It has been shown through laboratory experiments carried out on a scaled slip joint (see [33]), that a vibratory forcing allows for additional settlements in the same order of magnitude as observed in the full-scale case study, between 10–15 mm. Besides the evolution of the LVDT displacements, Fig. 7b shows the distribution of the relative displacement peaks measured during the reported events. For Fig. 7b, the relative values with respect to the monopile position are reported for each LVDT sensor, and with reference to a null starting condition for each event. Note that all the relative displacement peaks related to specific events (e.g. switching on/off the turbine blades, wind gusts, harsh waves) are all be below 1 mm.

3.2. Mechanical behaviour of the slip joint observed for chosen events

Besides the description of the long term variation of the hoop stresses and the displacements, few events will be chosen to showcase the distribution of the axial stress along the wind turbine tower and the monopile, the corresponding hoop stresses, and the behaviour of the first two bending mode shapes of the investigated structure during the selected event. The events are chosen to cover different operational loading conditions, such as the starting and the stopping of the blade rotation, and the mere presence of wind and wave loads (with the turbine being at standstill conditions). Some of the chosen events correspond to the start of the monitoring campaign, while others are taken from the end of the campaign. Note that for certain cases,

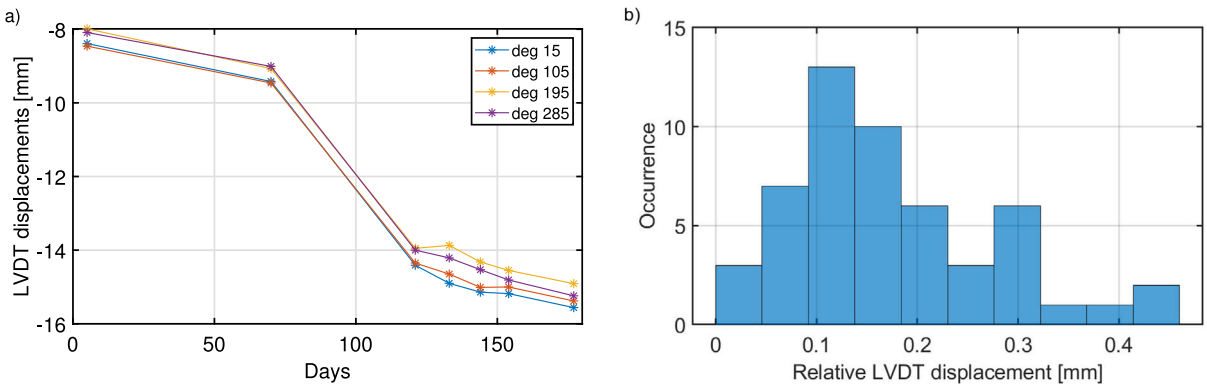

Fig. 7. LVDT displacements: (a) variation of the displacement through the monitoring campaign, measured by the LVDT sensors installed in S3 (see Fig. 2); (b) occurrence of the relative peak displacements that occurred during the selected event data set.

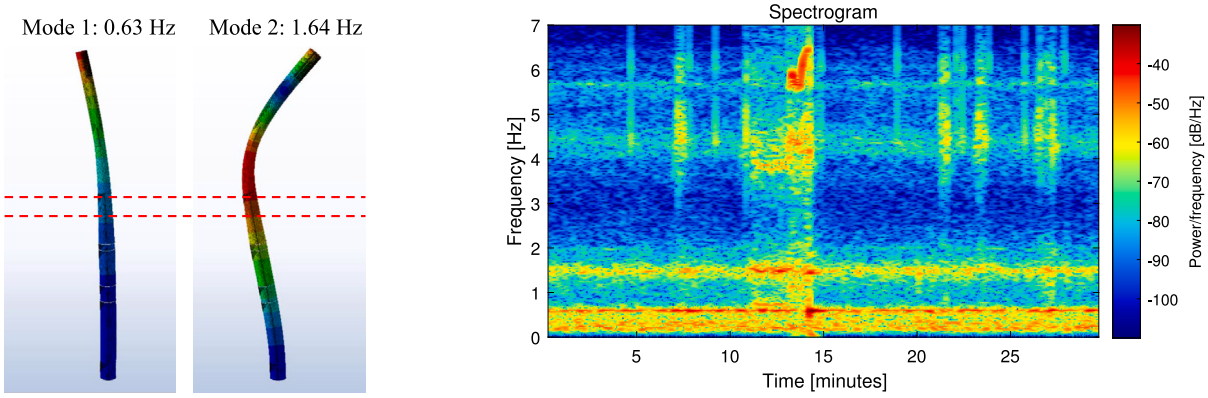

Fig. 8. (a) Estimated bending modes through a FE model, see [34], for a description of the FE model. The red dashed lines mark the location of the slip joint; (b) spectrogram of the event n. 01, estimated from a recorded acceleration time-series. (For interpretation of the references to colour in this figure legend, the reader is referred to the web version of this article.)

experimental data is simply missing due to faults in the sensing system, leading to empty spots in the following graphs.

The following graphs in Sections 3.2.2–3.2.4, present the axial stresses according to the azimuth angle heading described in Fig. 2, and are plotted from the lower position to the upper position, in which the height is referred with respect to the sea level. For the first described event, the data from the monopile and the wind turbine tower are separated. To simplify the presentation of the results, events are labelled from n. 01 to n. 04.

3.2.1. Event n. 01: behaviour of the first two bending modes

Event n. 01, already illustrated in Fig. 3, is characterized by time segments of rotating and standstill conditions of the blades. The behaviour of the first two bending modes of the investigated structure is highlighted, by post-processing the measured acceleration data through a short-time Fourier transform. Fig. 8a shows the estimated first two bending modes through a FE model developed and described in [34]. The red dashed lines in Fig. 8a, mark the location of the slip joint. The first fundamental bending mode occurs at 0.63 Hz, while the second mode is active around 1.64 Hz. Both frequencies are visible in Fig. 8b, that shows the results of the spectrogram, obtained by computing sequentially the short-time Fourier transform of time segments formed by 1024 data points each, over an event of 30 min. The sampling frequency of the acceleration data, from which the spectrogram was obtained, was 30 Hz. By inspecting the spectrogram, it can be observed that the two estimated modes at 0.63 Hz and 1.64 Hz are continuously active throughout the event, and significant changes do not occur before and after the period of blade rotation (11–15 min). The spectrogram also marks scattered amplitudes at frequencies between 0.2–0.3 Hz throughout the event, which could be most likely due to the wind excitation. During the rotation of the blades, approximately between minute 11 and 15, further frequencies are visible around 0.75 Hz and 1.2 Hz, which can be linked to the blade passing frequencies, that varies between 15 and 24 rpm. The origin of the frequency peaks observed between 4 Hz and 6 Hz are still unclear. However, their variation seems to follow the change of the rpm of the blades, but at the same time none of those frequency peaks is a multiple of the blade passing frequency.

3.2.2. Events n. 01–02: axial and hoop stresses due to the rotation of the blades

The behaviour of the axial and hoop stresses is investigated, while influenced by a loading condition driven by the rotation of the blades. This loading scenario is discussed for two different events, one with reference to event n. 01 (see Fig. 3), while the event n. 02 refers to a later stage of the monitoring campaign, specifically on the 02/03/2019 around 20:00. The purpose of this comparison is to assess whether the axial and hoop distribution may significantly change in time for a similar loading scenario.

Concerning event n. 01, the investigated time-instants are approximately marked by the vertical red lines shown in Fig. 3, which correspond to the main peaks of the axial stresses. These axial stresses measured at the lower tower of the wind turbine are shown in Fig. 9. The dashed horizontal lines indicate the upper edge of the monopile, while the dotted line marks the transition of the lower tower wall-thickness from 15 mm to 10 mm. The azimuth angle has as a reference the north direction, as indicated in Fig. 2, following a clockwise rotation. In general, the axial stress tends to decrease following a non-linear relation from the top to the bottom of the lower tower. The highest

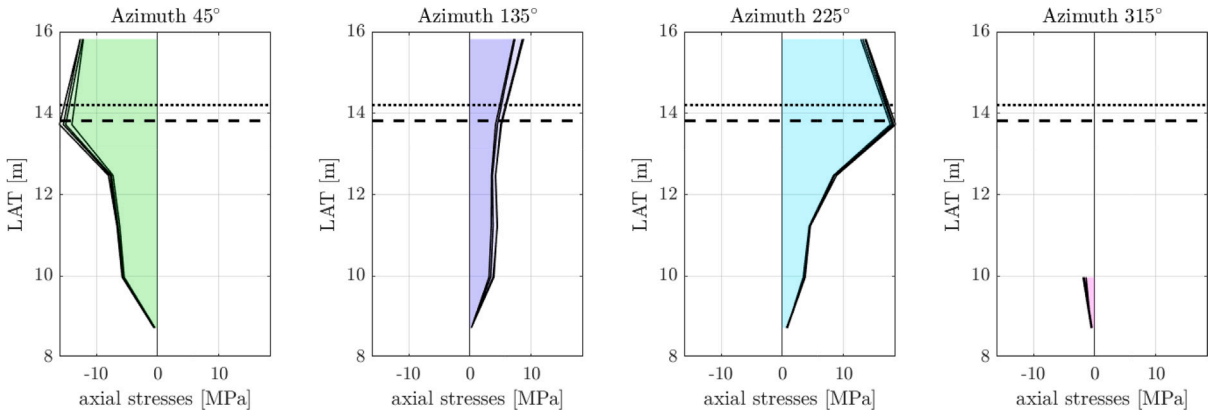

Fig. 9. Axial stresses on the lower tower for event n. 01 in selected times 838 s, 840 s, 843 s and 845 s. The dashed horizontal line presents the upper edge of the monopile. The dotted line presents the thickness change from 15 mm to 10 mm. The azimuth refers to the inclination from the north direction, as indicated in Fig. 2.

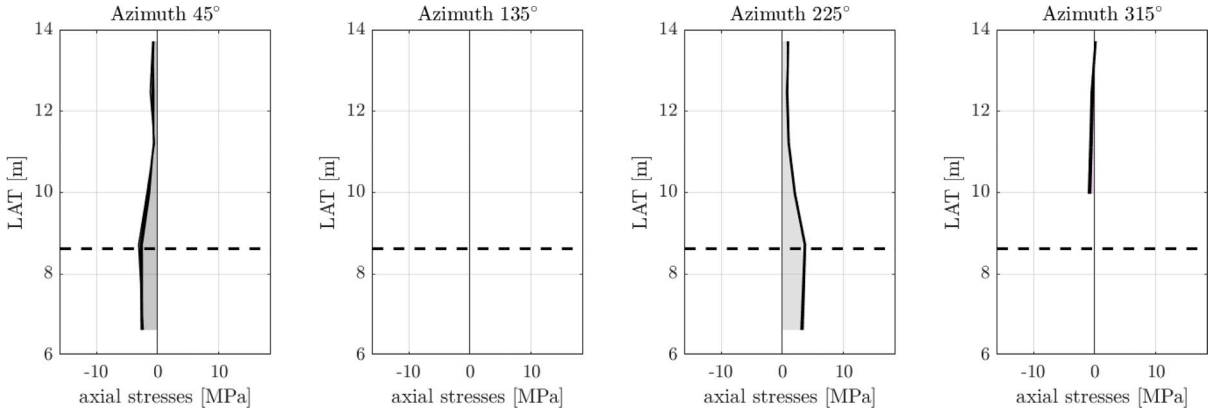

Fig. 10. Axial stresses on the monopile for event n. 01 in selected times 838 s, 840 s, 843 s and 845 s. The dashed horizontal line presents the lower edge of the lower tower. The azimuth refers to the inclination from the north direction, as indicated in Fig. 2.

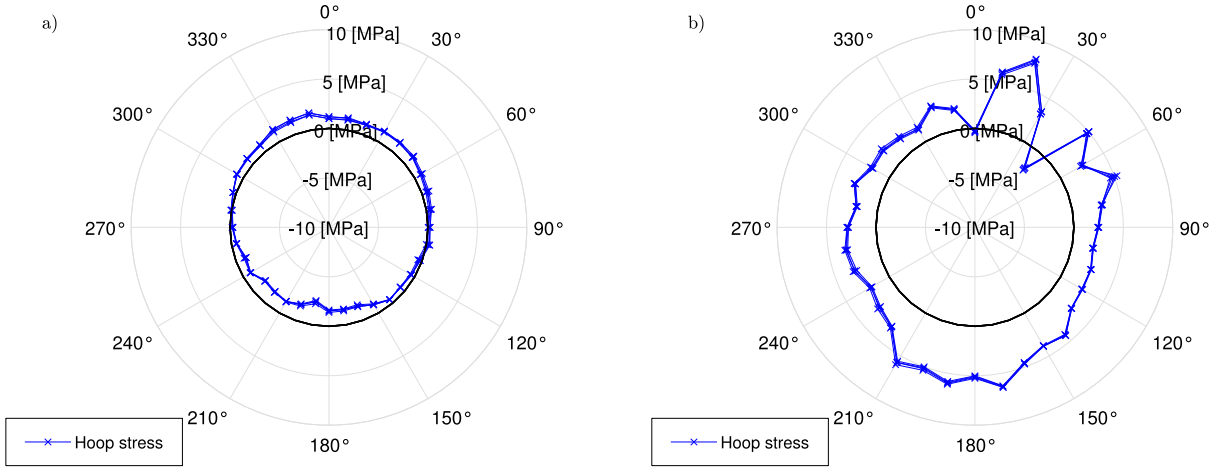

Fig. 11. Variation of the hoop stresses for event n. 01 in selected times 838 s, 840 s, 843 s and 845 s, for the instrumented cross section at (a) S9 (LAT09) and (b) S5 (LAT14).

peaks are observed along the azimuth 45° (in compression) and azimuth 225° (in tension), as soon the slip joint overlap starts at the top edge of the monopile. The measured relative axial peak stresses due to the blade rotations are around 16–17 MPa. Lower values of the axial stresses are observed for azimuth 135° and azimuth 315°, probably due to their proximity to the neutral axis of the cross-section. Fig. 10 showcases the relative axial stresses recorded along the monopile. The horizontal dashed line represent the lower edge of the lower tower. As expected, the values are generally lower, since the wall-thickness of the monopile is equal to 40 mm. It is worth mentioning, that the data from the sensors mounted on the monopile were often missing in a lot of positions, as highlighted in Fig. 10, therefore the axial stresses of the monopile will not be presented in the following events.

The relative peaks for the hoop stresses recorded during the rotation of the blades are shown in Fig. 11. It can be noted that for the lower cross-section, S9, the circumferential stresses are half in tension and half in compression, while the upper cross-section, S5, is entirely in tension. This behaviour could be explained by the presence of a

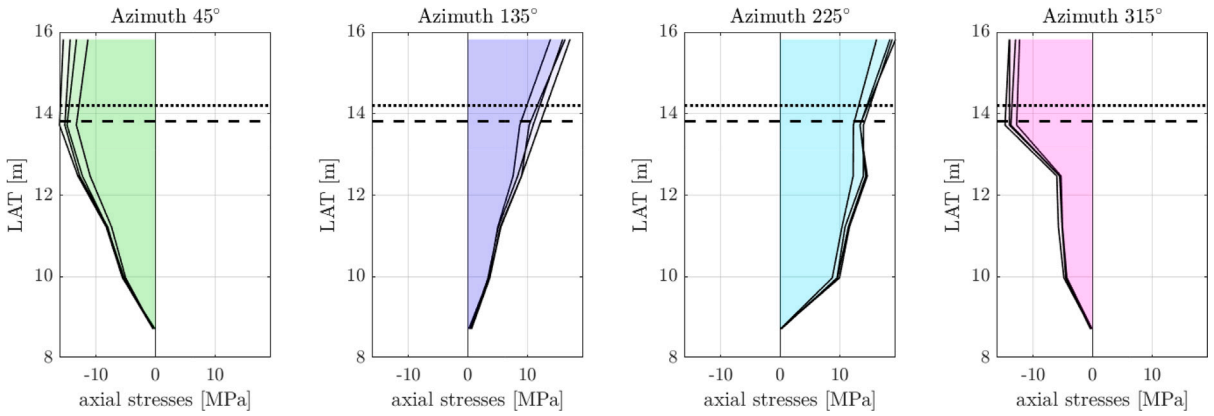

Fig. 12. Axial stresses on the lower tower for event n. 02 in selected times 1420 s, 1430 s, 1450 s and 1460 s. The dashed horizontal line presents the upper edge of the monopile. The dotted line presents the thickness change from 15 mm to 10 mm. The azimuth refers to the inclination from the north direction, as indicated in Fig. 2.

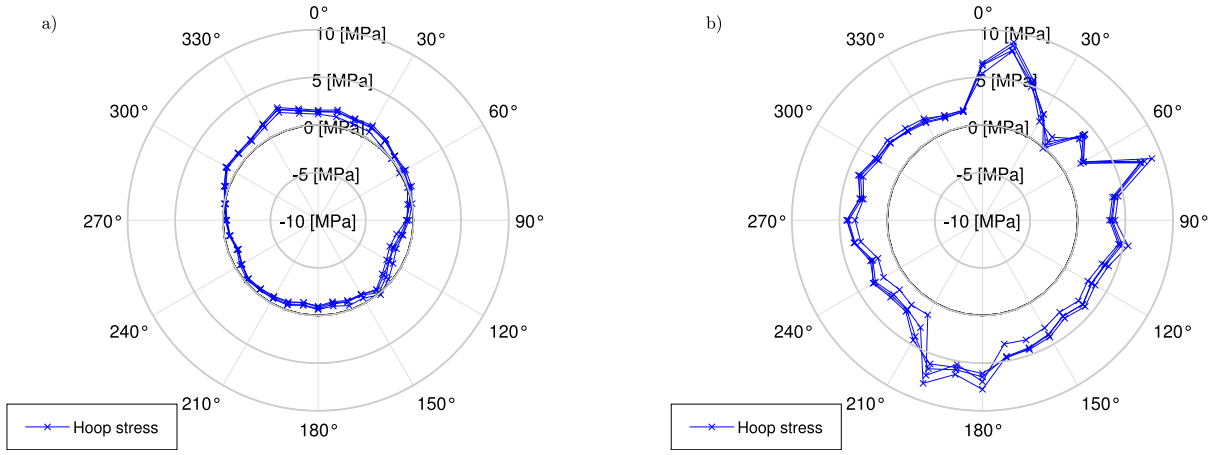

Fig. 13. Variation of the hoop stresses for event n. 02 in selected times 1420 s, 1430 s, 1450 s and 1460 s, for the instrumented cross section at (a) S9 (LAT09) and (b) S5 (LAT14).

bending moment and the consequent generation of contact gaps due to deformation of the lower tower. An attempt to explain this behaviour will be shown in Section 5. As a final remark, it is worth noting that the hoop stress amplitudes caused by the rotation of the blades, generally fall below 5 MPa for the case study at hand, which is rather low compared to the hoop stress induced by the installation process.

With reference to event n. 02, a similar behaviour for the relative peaks concerning the axial and hoop stresses can be observed. Fig. 12 shows the distribution of the axial stresses along the height of the slip joint, recorded on the surface of the lower wind turbine tower. The highest relative stresses are again observed along the azimuth 45° (in compression) and azimuth 225° (in tension). A first difference that can be observed, if compared with the axial stress distribution shown in Fig. 9, consists in slightly higher stress values recorded at LAT 15.82 during event n. 02, which sometimes exceed the axial stress values measured at LAT 13.72. A second difference is observable while inspecting the axial distribution for azimuth 135° and azimuth 315°, which reach higher values in Fig. 12. This could be due to a change of the orientation of the neutral axis, most likely oriented along the 90°–270° direction. The relative hoop stresses that correspond to the investigated axial stress peaks, are illustrated in Fig. 13, which exhibit a rather similar behaviour with respect to the stress distribution shown in Fig. 11. In fact, the upper cross section S5 is predominantly in tension, while cross section S9 is characterized by a tensile and compressive stress state. With reference to both events, relative axial and hoop stresses exhibit similar magnitudes and stress distribution, for a comparable loading condition occurring at different time instants.

3.2.3. Event n. 03: axial and hoop stresses due to different wind speeds

Event n. 03 occurred on the 09/02/2019 around 10:45, and showcases the relative axial and hoop stress distribution while the wind turbine was switched off and only environmental loading conditions were present (wind and waves). In Fig. 14, the stress state under two different wind speeds will be compared: the maximal wind speed at 30,4 m/s is presented by a solid line (Fig. 14a) and blue line (Fig. 14b), and the minimal wind speed at 14,1 m/s is presented by a dotted and dashed line (Fig. 14a) and red line (Fig. 14b). For both stress distributions, it can be observed that the stress magnitudes are rather small, around 1 MPa for the axial stresses and between 0–1 MPa for the hoop stresses. In general, the stress values seem rather similar, independently of the wind speed. It is worth mentioning though, that the relative stresses recorded under pure environmental and standstill conditions, were rather low and often overlapping with the background noise of the instrumented optical fibres. Due to the latter reason, no further data under the presented loading scenario is discussed.

3.2.4. Event n. 04: axial and hoop stresses recorded before, during and after a blade rotation period

Event n. 04 occurred on the 04/10/2018 around 18:15, and is characterized by multiple operating and standstill conditions of the blades. Fig. 15 illustrates an example of the behaviour in time of few selected axial stress measurements during the 30 min event, recorded at the cross-section S2. The investigated time instants refer to three different phases: phase 1 is marked by the red vertical dashed lines, (standstill condition); phase 2 is identified by the blue vertical dashed lines

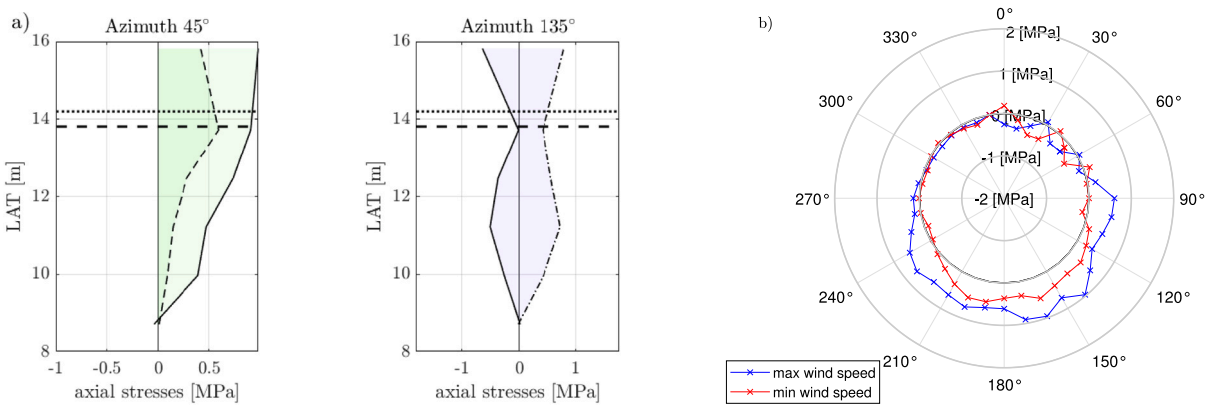

Fig. 14. (a) Axial stresses on the lower tower for event n. 03 in selected times 1523 s (solid line with wind speed = 30,4 m/s) and 1773 s (line with dot and dash presents speed = 14,28). The dashed horizontal line presents the upper edge of the monopile. The dotted line presents the thickness change from 15 mm to 10 mm. The azimuth refers to the inclination from the north direction, as indicated in Fig. 2; (b) variation of the hoop stresses for event n. 03 in selected times 1523 s (blue line) and 1773 s (red line), for the instrumented cross section S5 (LAT14). (For interpretation of the references to colour in this figure legend, the reader is referred to the web version of this article.)

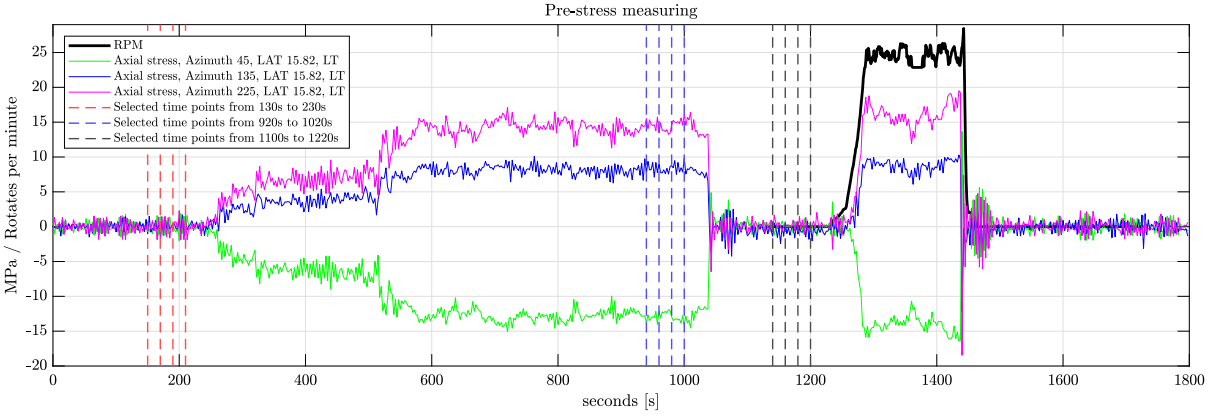

Fig. 15. Time behaviour of event n. 04, recorded on the 04/10/2018 around 18:15. Few examples of axial stress trends and the corresponding RPM of the blades are illustrated. LT stands for the lower tower of the wind turbine. (For interpretation of the references to colour in this figure legend, the reader is referred to the web version of this article.)

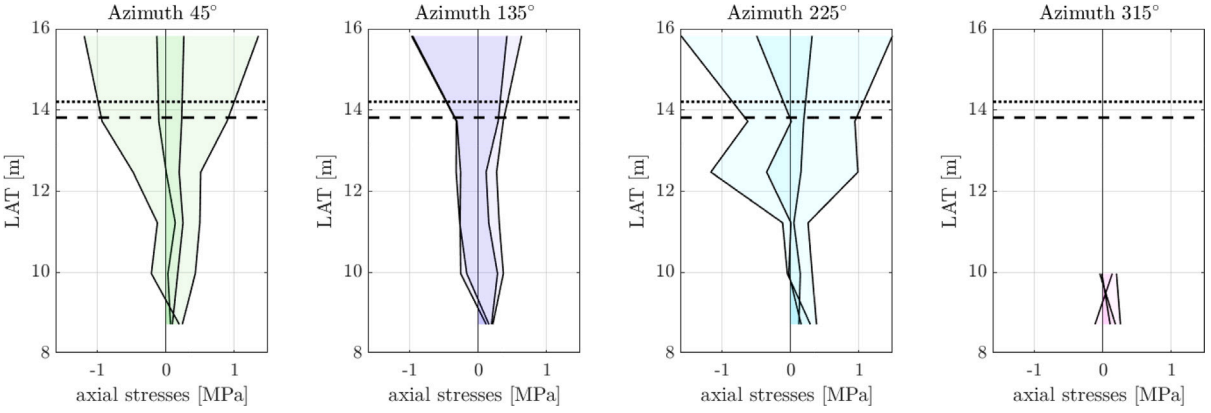

Fig. 16. Axial stresses on lower tower for event n. 04 in selected times 150 s, 170 s, 190 s, 210 s (in standstill condition, phase 1). The dashed horizontal line presents the upper edge of monopile. The dotted line present the thickness change from 15 mm to 10 mm. The azimuth refers to the inclination from the north direction, as indicated in Fig. 2.

(operational condition); and phase 3 by the black vertical dashed lines (standstill condition). Unfortunately, the available data concerning the rpm starts only after second 1000. However, from the operating day, it was possible to establish that the maximum rpm shown in Fig. 15, was also set during phase 2. The axial and hoop stress distribution for the lower part of the wind turbine tower, of each phase, are presented in Figs. 16, 17, 18, 19, 20, and 21. The standstill condition for the first and third phase were subject to similar loading conditions, characterized by a fairly constant wind speed of about 10 m/s.

As already shown and discussed in Section 3.2.3, the measured data corresponding to the phase 1 (standstill condition) show very small relative amplitudes of axial and hoop stresses, and no clear pattern in the stress distribution is observable, see Figs. 16–17. The stress state for the selected time instants of phase 1, seem to continuously switch from

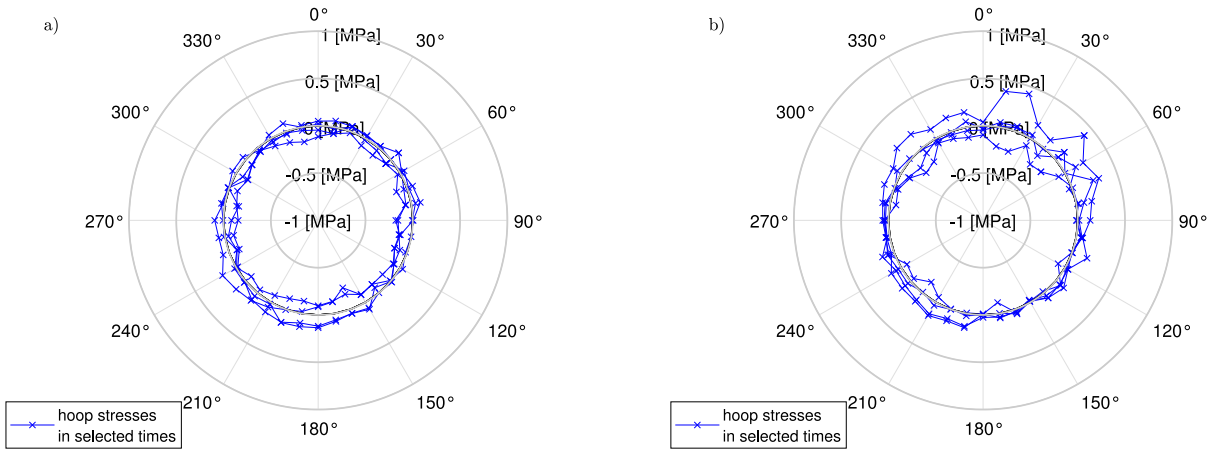

Fig. 17. Variation of the hoop stresses for event n. 04 in selected times 150 s, 170‘s, 190 s and 210 s (before the rotating of blades), for the instrumented cross section at (a) S9 (LAT09) and (b) S5 (LAT14).

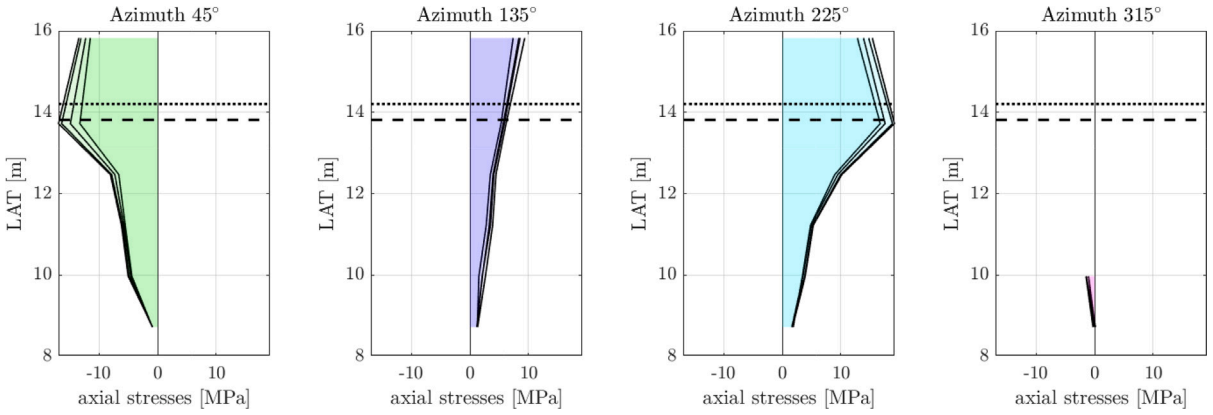

Fig. 18. Axial stresses on lower tower for event n. 04 in selected times 940 s, 960 s, 980 s, 1000 s (in rotating of blades). The dashed horizontal line presents the upper edge of the monopile. The dotted line presents the thickness change from 15 mm to 10 mm. The azimuth refers to the inclination from the north direction, as indicated in Fig. 2.

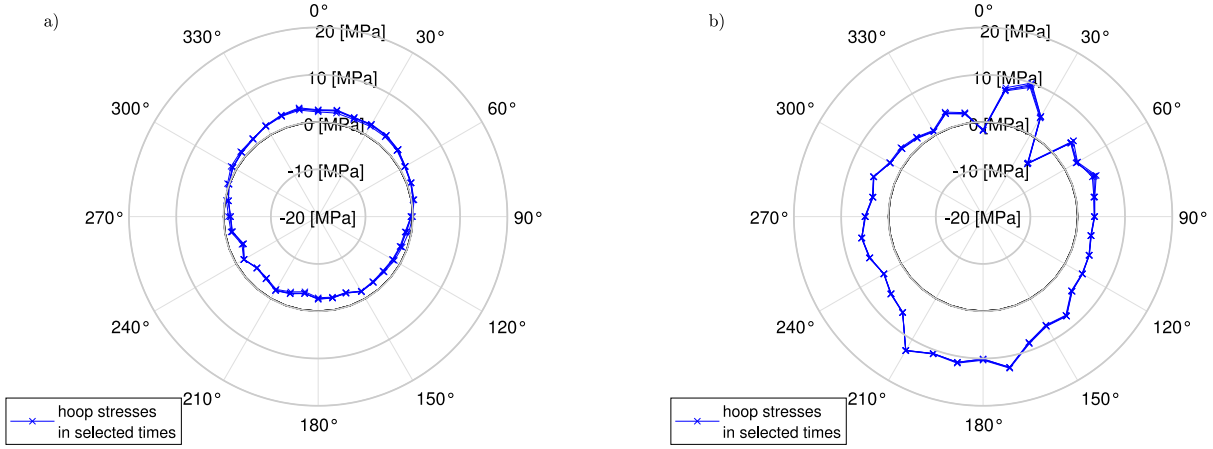

Fig. 19. Variation of the hoop stresses for event n. 04 in selected times 940 s, 960 s, 980 s and 1000 s (in rotating of blades), for the instrumented cross section at (a) S9 (LAT09) and (b) S5 (LAT14).

a tensile to a compressive state. This could be partly explained due to the low values of measured relative stresses that fall in the background noise level of the optical fibres. The second phase is characterized by an operational blade condition, and the axial and hoop stress distribution (see Figs. 18–19) is rather similar to the one observed and discussed in Section 3.2.2. As soon the wind turbine returns to a standstill condition (phase 3, see Figs. 20–21), some significant differences can be observed if compared to the stress state in phase 1. On one hand, the amplitudes of the axial stresses between phase 1 and phase 3 are quite similar and comparable, falling in the background noise of the optical fibres. On the other hand, the hoop stress values tend to remain higher in phase 3 compared to the ones observed in phase 1. The peak values of the hoop stresses reached 5 MPa in phase 3, whereas in phase 1, it was only about 0.5 MPa. What is more crucial, the stresses occurring in phase 3 retain almost 50% of the hoop stresses observed in the previous phase 2, preserving also a similar pattern. The measurement seem to indicate

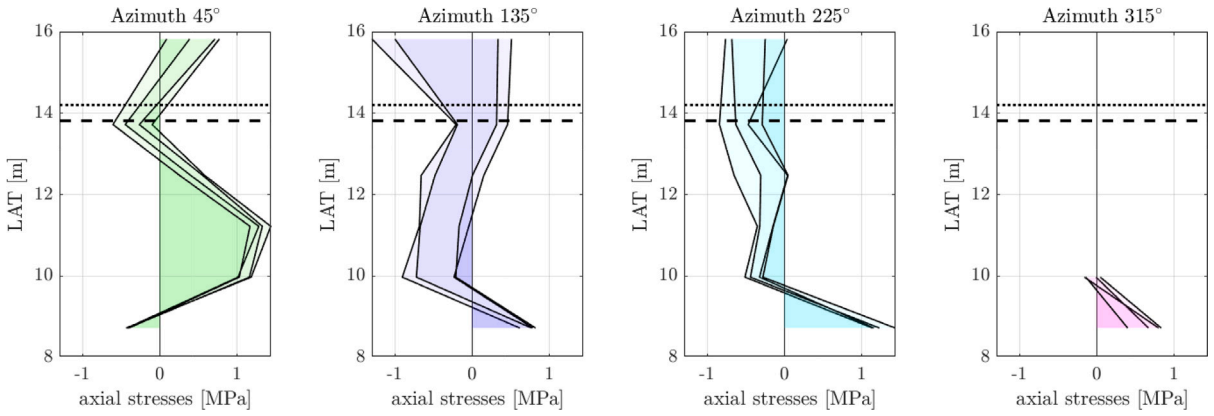

Fig. 20. Axial stresses on lower tower for event n. 04 in selected times 1140 s, 1160 s, 1180 s, 1200 s (after rotating of blades) The horizontal dashed horizontal line presents the upper edge of monopile. The horizontal dotted line presents the thickness change from 15 mm to 10 mm. The azimuth refers to the inclination from the north direction, as indicated in Fig. 2.

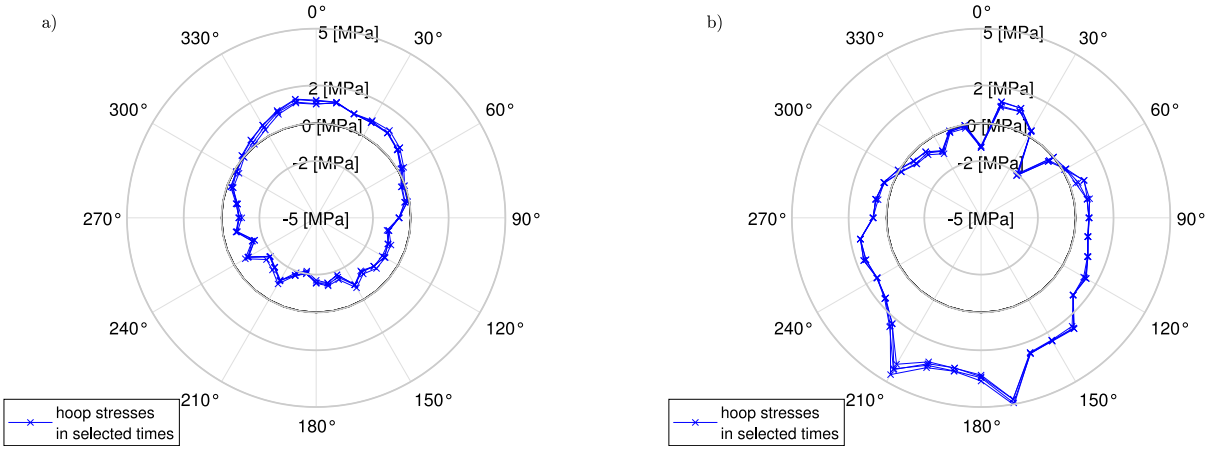

Fig. 21. Variation of the hoop stresses for event no. 4 in selected times 1140 s, 1160 s, 1180 s and 1200 s (after rotating of blades), for the instrumented cross section at (a) S9 (LAT09) and (b) S5 (LAT14).

that the hoop stresses are characterized by a sort of "memory effect", retaining a residual stress state from a previous loading condition, while the axial stresses seem to be independent of the loading history. By inspecting the relative displacement variation of the corresponding event, as depicted in Fig. 22, it is possible to understand the origin of such "memory effect" causing a residual stress state. The start of the event and throughout phase 1, is marked by an imposed "zero" displacement. The rotating condition in phase 2 generates an inclination of the lower tower, indicated by the two positive and negative displacement lines in Fig. 22. As soon the operational condition stops (after 1000 s), the lower tower is characterized by a residual displacement approximately around −0.1mm. This residual displacement indicates a temporary stick and settlement condition of the slip joint. As soon the blades are turned on again (after 1200 s), a further displacements occurs followed by residual displacement during standstill around −0.4mm. These small and temporary residual displacements, inevitably generate a state of prestress for the upcoming loading events.

4. Finite element model of the slip joint

4.1. Description of the FE model and the loading steps

The FE model was created using the commercial software Ansys 2020 [37]. The numerical model represents only a small part of the whole wind turbine structure, covering a sufficient area around the slip joint region, as shown in Fig. 23. The modelled area is chosen to ensure a uniform stress flow right before the slip joint, stemming from the load applied at the top of the model. The FE model consists of quadratic solid 3D elements (SOLID186) and contact elements (CONTA174) for the overlapping surfaces. The wall thickness was modelled through one solid element, characterized by a middle node and two external nodes throughout the thickness. The type and size of the elements were chosen through a sensitivity analysis by iteratively changing the mesh type and size. The final element size was set to 100 mm for the overlapping zone and 150 mm for the area above and below the slip joint. The contact interaction between the overlapping surfaces was set up as frictional, characterized by a coefficient of friction equal to 0.3. The contact interaction is tackled through an Augmented Lagrange method, an available routine in Ansys. The initial gap between the overlapping surfaces was set to 0, assuming a contact surface without manufacturing imperfections. The reason behind this choice stems from the lack of knowledge concerning the actual surface imperfection of the investigated slip joint. The model was interrogated through a nonlinear static analysis by using an iterative solver based on the unsymmetrical Newton Raphson technique present in Ansys. In total, the model consists of 151631 nodes and 453693 degrees of freedom. External forces were applied on a 40 mm rigid plate included on the upper part of the model, in order to uniformly transfer the stresses to the structure. The bottom part of the model was assumed to be rigidly fixed on a fictitious ground.

For the nonlinear static analysis, a vertical load acting along the longitudinal axis of the structure (see FVF1, green line in Fig. 23) was chosen, and three horizontal loads acting along different directions (see FHF1-3, red vectors in Fig. 23). Since it is not possible to accurately

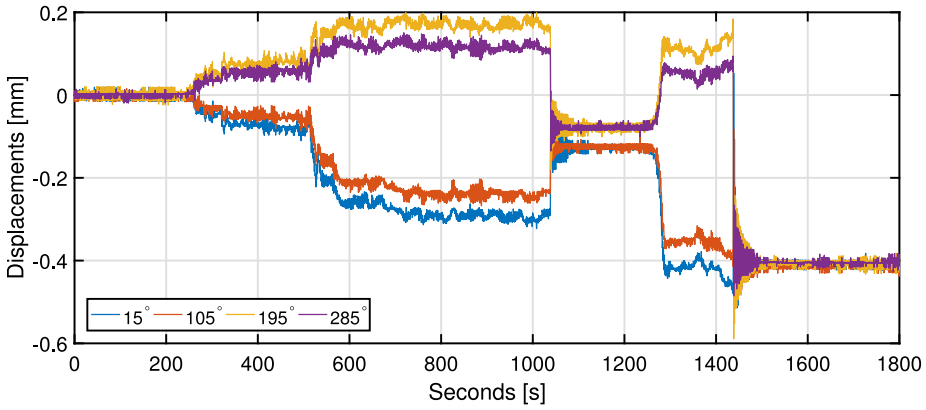

Fig. 22. Variation of the displacements recorded at event n. 04. (For interpretation of the references to colour in this figure legend, the reader is referred to the web version of this article.)

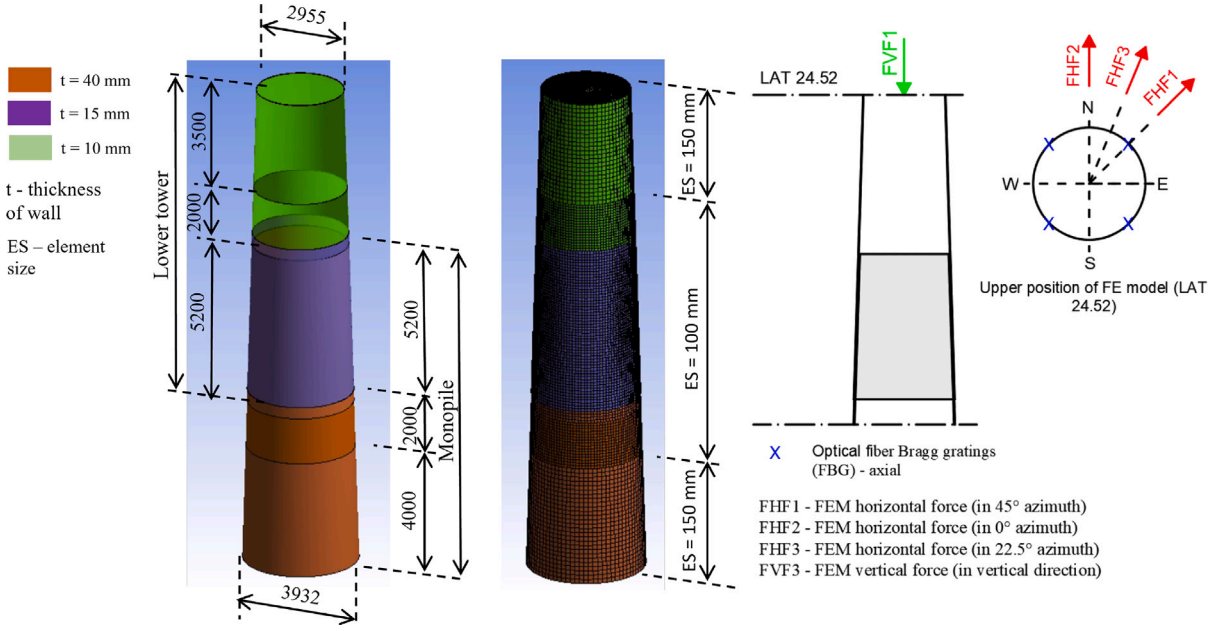

Fig. 23. Schematic representation of the different parts of the FE model, visualization of the mesh and description of the applied loads.

determine a precise loading direction from the experimental data, the FE model was interrogated by assuming three different horizontal loads, located between two optical fibre sensors used to measure the axial strains. Such horizontal loads were applied separately during the nonlinear static analysis, and a comparison with the experimental data is shown in Section 5.

4.2. Base verification of the slip joint FE model

The verification of the FE model is performed by comparing the stress calculated by three simplified analytical approaches with the corresponding estimated stresses by the FE model. Eq. (1) is used to compute the hoop stress due to a vertical load FVF1 (excluding the presence of external moments) at cross section S5, while the axial stress due to FVF1 at cross sections S2 and S11 is simply computed by the ratio between the vertical load and the annular area. The axial stress caused by an applied horizontal force is also computed by

$$\sigma_{axial} = \frac{FHF * r}{W_r} \quad \left[\frac{\mathrm{N}}{\mathrm{m}^2}\right] \tag{2}$$

where FHF represents the horizontal force, r defines the distance from the applied force to the selected cross-section, and W_r stands for the section modulus. The needed values for Eq. (2) are shown in Table 1.

Table 1
Parameters for Eq. (2).

LAT [m]	r [m]	W_r [m^2]	FHF [kN]
15.82	3.5	0.078	5000
6.62	12.7	0.427	5000

Table 2
Hoop and axial stresses from the FE model for model verification. LT stands for lower tower, while MP for monopile.

$Force$ [kN]	$\sigma_{hoop,S5}$ [MPa]	$\sigma_{axial,S2}$ [MPa]	$\sigma_{axial,S11}$ [MPa]
FVF1 = 870	5.38 (LT)/2.02 (MP)	9.4	1.8
FHF1-3 = 5000	–	224	149

Table 2 summarizes the computed axial and hoop stress according to the above-mentioned analytical formulas. Note that the loads are applied independently, no stresses resulting from a concurrent effect of both vertical and horizontal loads are computed.

The hoop and axial stresses shown in Table 2, are then compared to the corresponding ones estimated by the FE model, as shown in Fig. 24. The solid lines refer to the stresses estimated on the lower tower, while the dashed line refers to the stress computed on the monopile. The

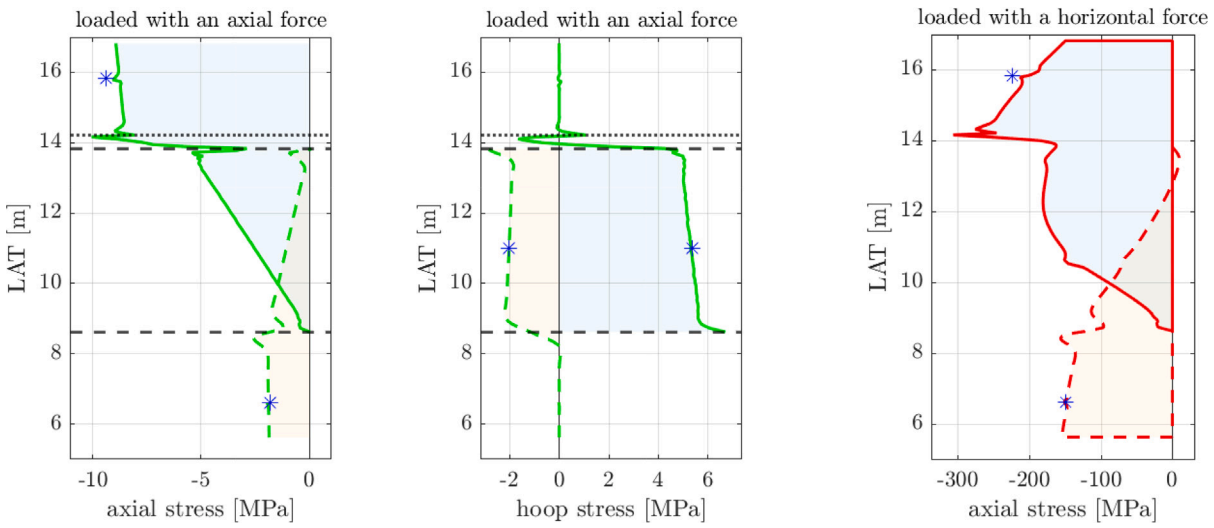

Fig. 24. Results of the FE model verification. The solid line presents the computed stresses on the lower tower, and the dashed line presents the stresses on the monopile. The blue stars indicate the analytical values according to the Table 2, while the green and red colour refer to the stress due to an axial load and horizontal load, respectively. (For interpretation of the references to colour in this figure legend, the reader is referred to the web version of this article.)

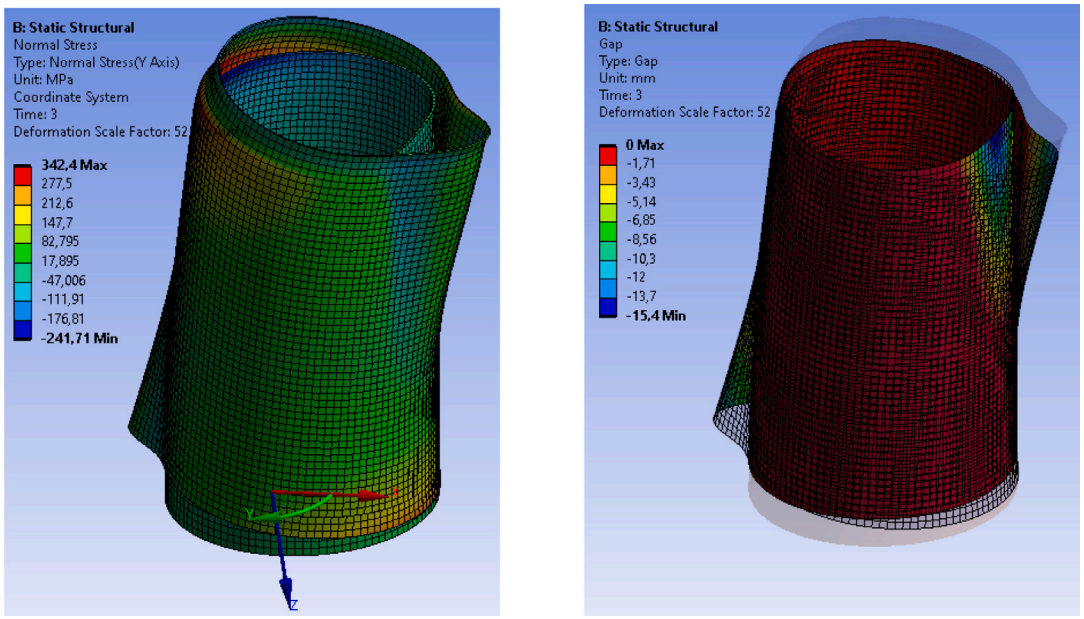

Fig. 25. On the left hand side, hoop stresses are presented. On the right hand side, the gap between the monopile and the lower tower is presented.

blue stars are the stresses presented in Table 2, while the green and red colour refer to the stresses computed by the FE model due to an axial load and horizontal load, respectively. Note that the same colour and line type notation is kept throughout the remaining part of the paper. The comparison shows that the FE model behaves according to the analytical results.

4.3. Axial and hoop stress distribution obtained from the FE model

Fig. 25 graphically illustrates the 3D deformation of the FE model due to a horizontal load of FHF1, specifically focusing on the hoop stress (left figure) and the contact gap caused by the applied load (right figure). It can be noted that hoop stresses are almost uniform and in tension as long the surfaces are in contact, while a transition between compressive and tensile behaviour occurs in areas characterized by a contact gap. The application of an horizontal load, assuming an initial ideal contact area with no surface imperfections, leads to two areas characterized by a contact gap: a top and bottom area, opposite to each other (see right graph in Fig. 25).

The predictions of the FE model are mainly tailored to the mechanical response of the lower tower, since the experimental data for the monopile are rather scarce due to sensing faults. Fig. 26 shows the axial stress distribution over the height of the slip joint at the lower tower's surface, plotted according to the sensor layout and for different orientation of the horizontal force (see different red lines in Fig. 26). The overlapping area is confined by the two horizontal black dashed lines. Two features are clearly observable: (a) axial stress peaks occur between the wall thickness change (horizontal black dotted line) and the upper edge of the monopile (black horizontal dashed line); (b) within the overlapped surfaces, the decreasing trend of the axial stress depends on the direction of the horizontal force. For the chosen sensing point, a linear decrease of the axial stress is only observable if the horizontal load is exactly applied in between two sensing points (Azimuth 0°, see Fig. 23). Fig. 27 presents the axial stress distribution

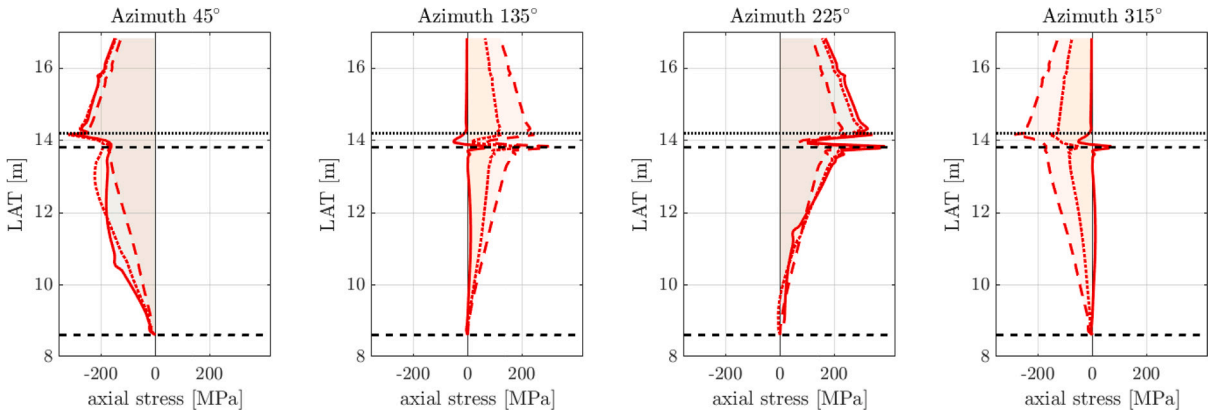

Fig. 26. Axial stresses on the lower tower caused by separate forces FHF 1 (red solid line), FHF2 (red dashed line), and FHF3 (red dotted line) that are equal to 5000 kN. The results are presented in vertical paths for selected azimuths. The black horizontal dashed line defines the overlapping region of the slip joint. The black horizontal dotted line presents the thickness change from 15 mm to 10 mm. The azimuth refers to the inclination from the north direction, as indicated in Fig. 2. (For interpretation of the references to colour in this figure legend, the reader is referred to the web version of this article.)

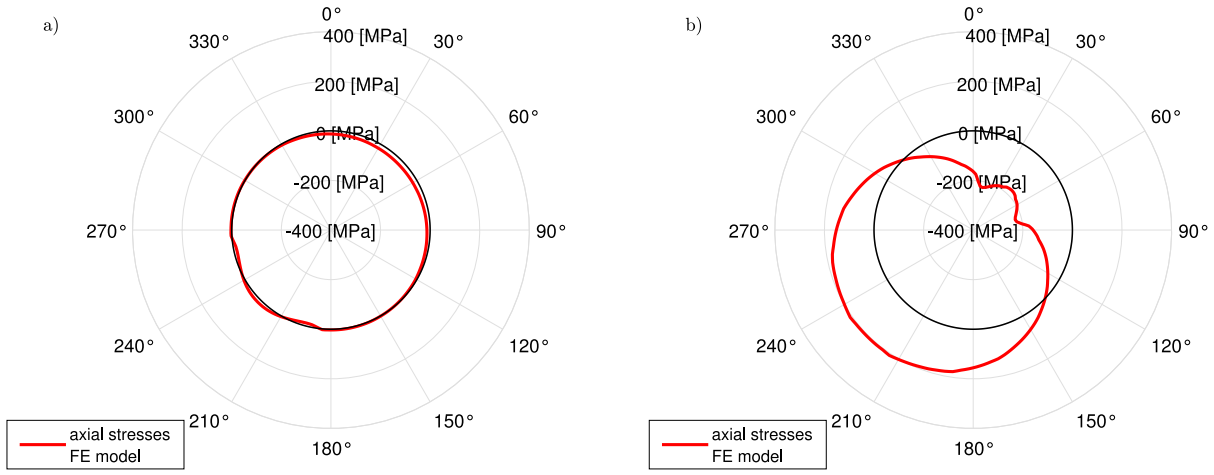

Fig. 27. Variation of the axial stresses caused by FE force FHF1 (5000 kN) for the instrumented cross section at (a) S9 (LAT09) and (b) S5 (LAT14).

in a polar reference frame, for cross section S9 and S14. On one hand, it can be observed that the axial stresses almost disappear in the lower cross section S9, because the axial stresses are almost entirely transferred to the monopile. On the other hand, as expected, the axial stress are partly in tension and compression at cross-section S14, due to the applied bending moment.

Figs. 28 and 29 depict the hoop stresses variation along the height of the slip joint and along the circumference of cross section S9 and S14. As mentioned above, the horizontal loads are applied between azimuth 0° and 45°, hence a significant difference of the hoop stress between the vertical path at azimuth 45° and azimuth 225° is expected, as demonstrated in Fig. 28. On one hand, at azimuth 45°, which direction is nearby the horizontal load direction, low values of the hoop stress are observed at the top of the slip joint, where the contact gap occurs, and higher values occur at the bottom part which is characterized by a full contact between the two overlapping surfaces. On the other hand, at azimuth 225°, higher tensile hoop stresses are visible at the top part of the slip joint (contact area), while smaller tensile and compressive hoop stresses are detectable at the bottom part (contact gap). As stated above, whenever contact gaps occur, a transition between small tensile and compressive stresses occur. This is clearly visible in Fig. 29 as well. The reason of such transition, is due to the presence of a local bending moment along the segment of the shell plate characterized by the presence of the contact gap. Along an approximately perpendicular plane with respect to the loading direction, the variation of the hoop stress is fairly similar as shown in Fig. 28, for azimuth 135° and 315°: a nonlinear trend of the hoop stress variation is observed, where high tensile hoop stresses are noticeable at the top and bottom part of the slip joint, approaching smaller values in the middle zone.

Based on the deformed behaviour shown in Fig. 25, and the axial and hoop stress variation shown in Figs. 26–29, on may deduce that the bending moment is transported from the upper to the lower part of the slip joint through two mechanisms. The first mechanism is based on the frictional shear stresses between the two overlapping cones, for which axial stresses decreases from the upper to the lower part of the lower tower. The second mechanism is based on the geometrical contact constraint of the overlap between the two cones. In fact, as shown in Fig. 25, due to an horizontal load, two opposite contact areas are formed in the slip joint, which also generate normal stresses. These contact areas are captured in Figs. 28–29, and located wherever high tensile values of the hoop stress occur. These mechanisms of transmitting the bending moment were also hypothesized in [36] by suggesting simplified analytical expressions, and confirmed here throughout a numerical model.

5. Comparison

5.1. Comparison between FEM results and experimental data

This section compares the experimental data and the simulated results obtained from the FE model (FEM). The experimental data are

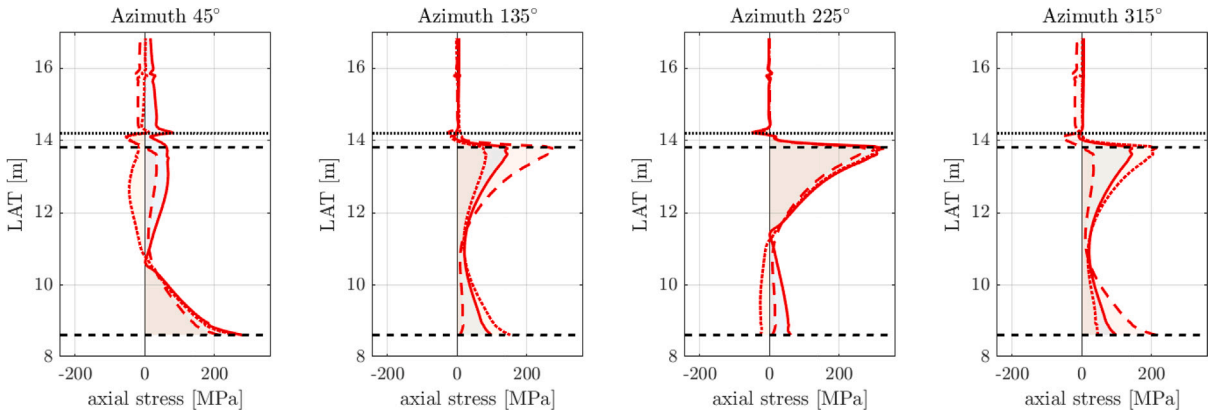

Fig. 28. Hoop stresses on the lower tower caused by separate forces FHF 1 (red solid line), FHF2 (red dashed line), and FHF3 (red dotted line) that are equal to 5000 kN. The results are presented in vertical paths for selected azimuths. The horizontal dashed horizontal line presents the upper edge of monopile. The horizontal dotted line presents the thickness change from 15 mm to 10 mm. The azimuth refers to the inclination from the north direction, as indicated in Fig. 2. (For interpretation of the references to colour in this figure legend, the reader is referred to the web version of this article.)

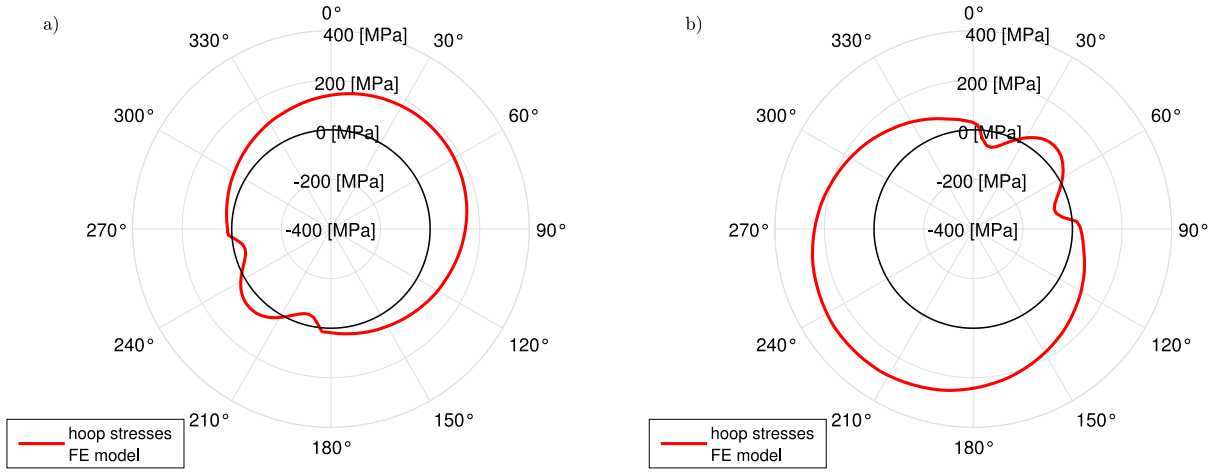

Fig. 29. Variation of the hoop stresses caused by FE force FHF1 (5000 kN) for the instrumented cross section at (a) S9 (LAT09) and (b) S5 (LAT14).

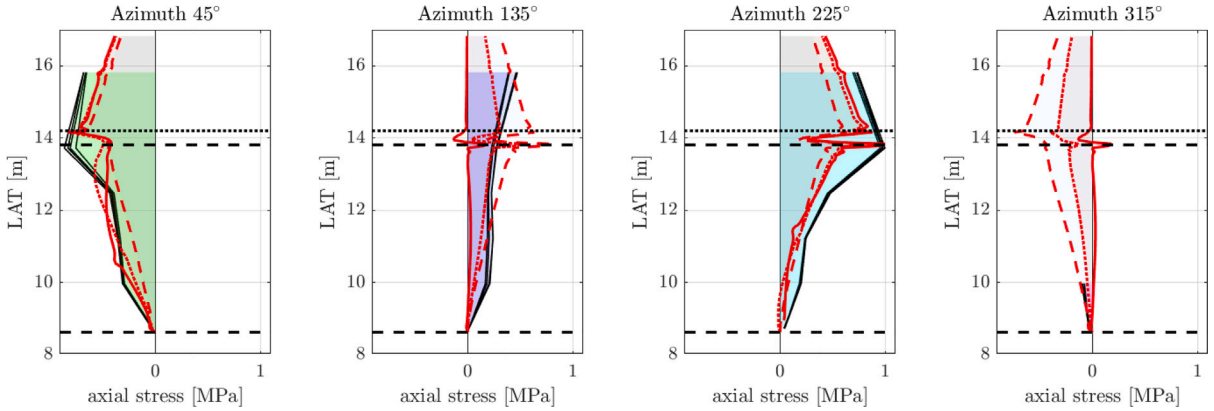

Fig. 30. Comparison of axial stresses between measured data (event n. 01) and FE data on the lower tower of the wind turbine. The red lines refer to the FEM results, for different horizontal loads, while the black lines refer to the experimental results. (For interpretation of the references to colour in this figure legend, the reader is referred to the web version of this article.)

normalized to their maximum value, while the FEM results are normalized with respect to the amplitude that corresponds to the location of the maximum experimental value. As already mentioned throughout the paper, the experimental data are only available at certain points, therefore, they cannot fully capture the extreme changes in behaviour observed in the FEM simulations. Hence, this comparison focuses on the qualitative trend of the axial and hoop stress variation observed thanks to the monitoring campaign. As shown in Section 4, the comparison is limited to the stresses observed in the lower tower of the wind turbine. The axial and hoop stress for event n. 01 are presented in Figs. 30–31, while the Figs. 32–33 refer to event n. 02.

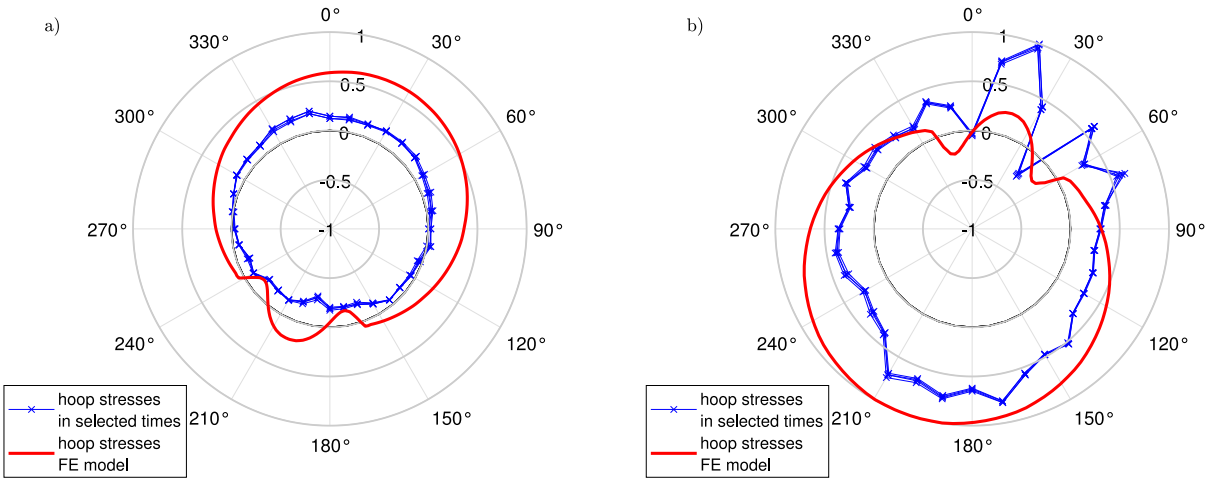

Fig. 31. Comparison of hoop stresses between measured data (event n. 01) and FE data on the lower tower of the wind turbine, for the instrumented cross section at (a) S9 (LAT09) and (b) S5 (LAT14). The red and blue line refer to the FEM and experimental results, respectively. (For interpretation of the references to colour in this figure legend, the reader is referred to the web version of this article.)

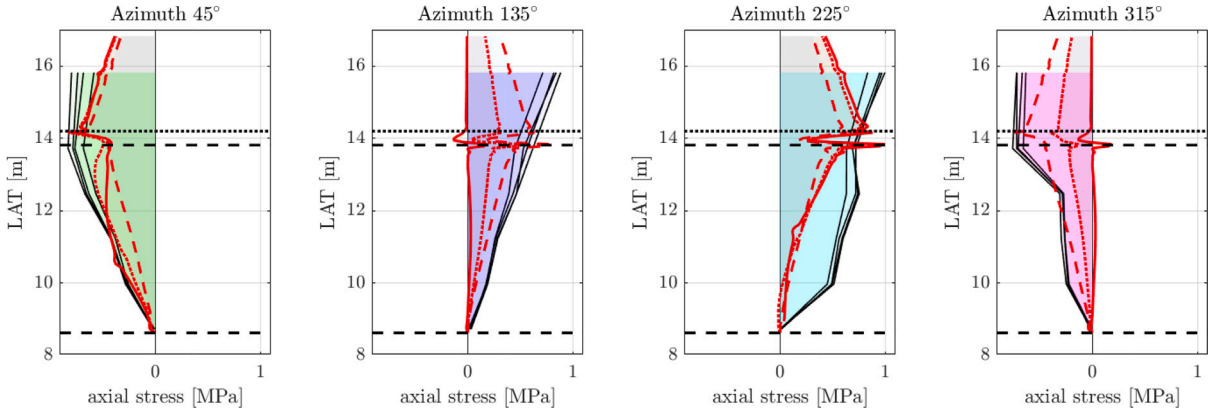

Fig. 32. Comparison of axial stresses between measured data (event n. 02) and FEM data on the lower tower of the wind turbine. The red lines refer to the FEM results, for different horizontal loads, while the black lines refer to the experimental results. (For interpretation of the references to colour in this figure legend, the reader is referred to the web version of this article.)

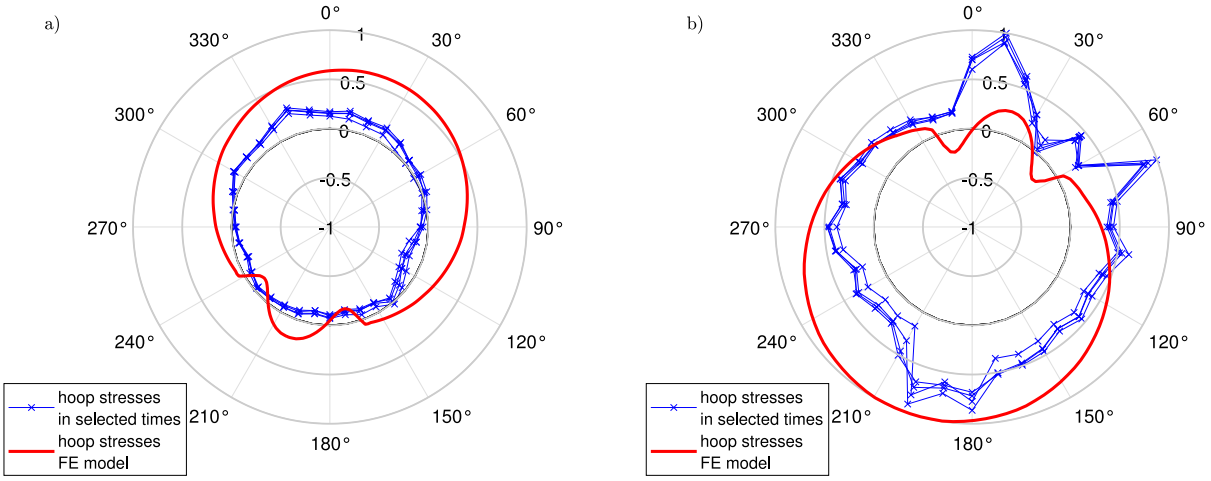

Fig. 33. Comparison of hoop stresses between measured data (event n. 02) and FE data on the lower tower of the wind turbine, for the instrumented cross section at (a) S9 (LAT09) and (b) S5 (LAT14). The red and blue line refer to the FEM and experimental results, respectively. (For interpretation of the references to colour in this figure legend, the reader is referred to the web version of this article.)

Since the comparison is referring to specific events, the FE simulation starts by including only the horizontal loads, as discussed in Section 4. In comparing axial stresses (see Figs. 30 and 32), the measured axial stresses follow rather well the expected behaviour of the FE model, transferring the stresses from the lower tower to the monopile. Some discrepancies can be observed for the simulated and

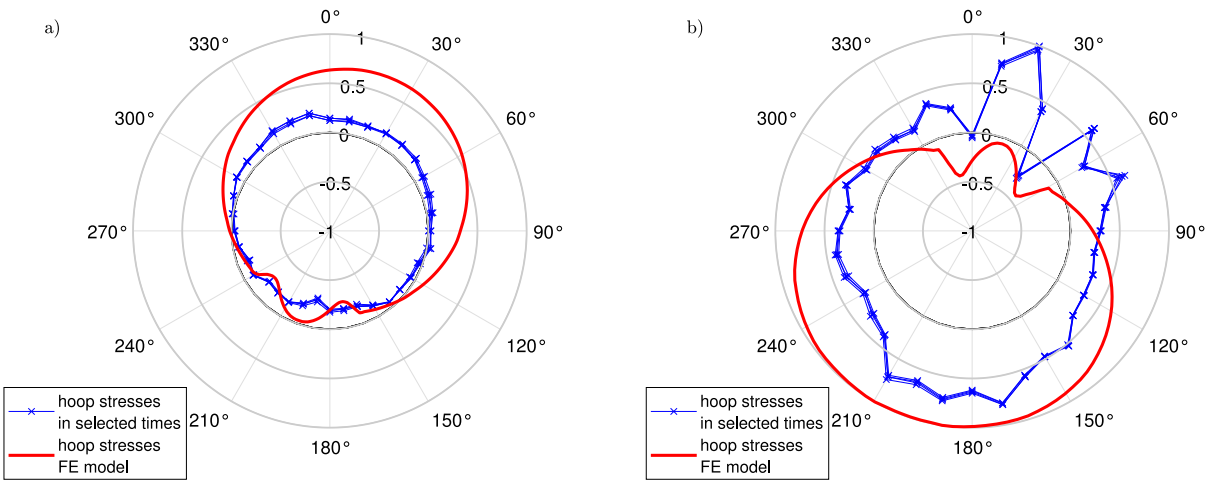

Fig. 34. Comparison of the hoop stresses between measured data (event n. 01) and FE data (pretension) on the lower tower of the wind turbine, for the instrumented cross section at (a) S9 (LAT09) and (b) S5 (LAT14). The red and blue line refer to the FEM and experimental results, respectively. (For interpretation of the references to colour in this figure legend, the reader is referred to the web version of this article.)

measured data at azimuth 225° in Fig. 32, where the experimental data seems to exhibit higher values. Despite such discrepancy, the pattern of the experimental data are closer to the simulated data corresponding to the two red dashed and dotted lines. Therefore, it may be possible to infer the direction of the horizontal load, somewhat between the direction of FHF2 and FHF3 (see Fig. 23), which lies between two instrumented points. Contrary to what observed for the axial stress, the comparison concerning the hoop stresses is not as satisfactory. At cross-section S9 (see left plot of Fig. 31 and Fig. 33), almost half of the circumference is in compression, while the other half is in tension. The FEM results show only two short lengths in compression. One may conclude that this could be due to the lack of modelling the surface imperfections, hence missing eventual contact gaps in the FE model. However, the scope of this work is to assess an ideal FE model, without imperfections. Therefore, in the next subsection the focus is on the effect induced by including a prestress in the FEM model, following the observation made in Section 3.2.4.

5.2. Effect induced by a prestress on the hoop stress

Section 3.2.4 pointed out the possibility of the slip joint's hoop stress exhibiting a kind of "memory effect", stemming from the loading history. The various loads, such as the dead loads or bending moments generated by rotating blades or wind gusts, could induce a state of pretension in the hoop stresses. In the FEM analysis, the vertical force FVF1 (870 kN) can generate the pretension of the slip joint. This force includes the self-weight of the part above the slip joint. Hence, the loading sequence for the FEM analysis, consists in first applying the dead load (FVF1), followed by an horizontal force equal to 75 kN and oriented along the 20°–200° direction. This direction was determined according to the experimental hoop stress pattern. Figs. 34 and 35 compare the normalized experimental hoop stresses and the corresponding FEM results inclusive of a pretension state. The hoop stress graphs were obtained subtracting the hoop stress from phase 1, characterized by the presence of the vertical force, from the results of the hoop stress in phase 2, characterized by both vertical and horizontal force. The reason behind this approach is to exactly mirror the available experimental data for each event, which were nulled at the beginning of the event's data set.

The introduction of a pretension due to the vertical load, changes the behaviour of the hoop stress along the chosen cross-sections. By applying the pretension, it is possible to see that a part of the circumference is in compression and the remaining part exhibits a tensile stress state. This phenomenon was also seen in the experimental data, see Fig. 11a and Fig. 13a, where for the instrumented cross-section at S9 it is possible to see that half of the circumference is in compression and the other one is in tension. In this case, it is important to note that the effect of a pretension on the hoop stress pattern, depends on the ratio between the applied vertical and horizontal force. The choice of a horizontal force equal to 75 kN, is dictated by the observation that such magnitude generates similar axial stresses as those reached during the rotation of the blades for the chosen events. By increasing the horizontal force, the pattern of the hoop stress gradually approaches the ones shown in Figs. 31 and 33.

6. Discussion and conclusions

6.1. Discussion and future work

Throughout the paper, the comparison between FEM results and measured stresses highlighted some patterns and trends that could be fairly reproduced through an ideal slip joint model. Specifically, the axial stress variation along the slip joint shows a satisfactory match with the numerical model, and some experimentally observed hoop stress variation caused by an horizontal force are also visible in the simulated results. On top of that, the simplified analytical expression of the hoop stress shown in Eq. (1) allows to shed light on the percentage of the contact area and the possible coefficient of friction needed, to qualitatively match the hoop stresses observed after 16 h of the installation. It was shown in Fig. 6 that a reduced contact area and a low coefficient of friction, leads to a fairly good match in terms of reached hoop stress amplitudes. At the same time, experiments also showed that a FE model of a slip joint characterized by an ideal overlap and contact area, is not able to fully reproduce the hoop stress pattern occurring along the circumference of any slip joint's cross section. This was clearly highlighted in Fig. 5, which hoop stress pattern is characterized by a somewhat "corrugated-like" shape, exhibiting transitions between a compressive and tensile stress state. It was shown through the FE analysis, see Fig. 29 for example, that such transitions could be explained through the presence of eventual contact gaps in the overlapped area of the slip joint. Note that no attempt was made in this study to assume a possible configuration of manufacturing imperfections of the overlapping cones, since the inference of such geometrical imperfection from the available experimental data constitutes an ill-posed inverse problem, leading to multiple possible contact configurations. A further interesting observation was made concerning the first high stress peaks (200 MPa in one location) reached right after the installation process. It is possible to assume that the reason for such high stress state is due

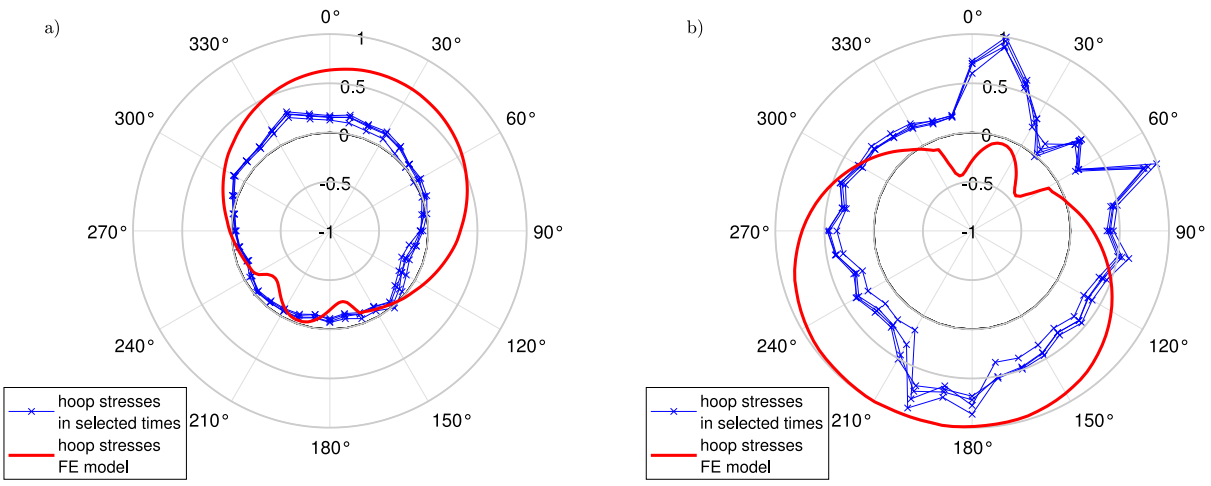

Fig. 35. Comparison of hoop stresses between measured data (event n. 02) and FE data (pretension) on lower tower of the wind turbine, for the instrumented cross section at (a) S9 (LAT09) and (b) S5 (LAT14). The red and blue line refer to the FEM and experimental results, respectively. (For interpretation of the references to colour in this figure legend, the reader is referred to the web version of this article.)

to the reduced and early-stage contact area reached at beginning of the installation process.

A further relevant finding was discussed in Sections 3.2.4 and 5.2, in which the importance of the prestress is highlighted. It is essential to note that the displacements induced after the installation process will form a state of prestress that remains their during the whole monitoring campaign. Such initial prestress governs any further stress variation caused by upcoming events. Besides the installation process, additional prestress (but smaller in amplitude) appear after significant loading events that may cause a residual settlement/displacement in the slip joint, as shown in Section 3.2.4. Such residual displacements are inherently linked to the actual surface imperfection and to the frictional behaviour of the surfaces. This finding implies that to correctly model the slip joint behaviour, it is essential to know the loading history and identify events that may cause residual displacements. Such settlements translates into a temporary "stick" condition, which can change to a different contact configuration only through loads that exceed the eventual static friction of the two overlapping surfaces.

It is worth mentioning that differential displacements were not reproduced throughout the FE model, since they inherently depend on the initial contact gaps occurring right after the installation process. Fig. 7 shows the evolution in time of the settlements and the various smaller differential displacements occurring for different intermediate events. Note that the initial achieved overlap right after the installation was around 5.19 m, compared to the desired target of 5.20 m. The missing 10 mm, are covered within the first 50 days, while the remaining displacement is a consequence of the successive events that induced small and residual differential displacements. As mentioned earlier, this residual displacement due to significant loading events, contribute to a state of prestress for upcoming loading events, which should be taken into account in any attempt to accurately capture the mechanic behaviour of a slip joint.

Despite some open modelling challenges, the slip joint has the potential to become a valid alternative to connect support structures and wind turbine towers. The installation time is far lower compared to traditional connections made out of grout or bolts. In addition, the slip joint may also proof beneficial as a seafastening solution on vessels to tackle upcoming offshore transportation challenges, since wind turbine structures keep increasing their size. Future research lines for the slip joints are rather intuitive to foresee. To keep the discussion short, examples of such research lines limited to the "quasi-static" behaviour are discussed. For example, a more detailed numerical model, inclusive of pre-measured surface imperfections, should be developed and validated against experimental results, interrogating the model to predict axial and hoop stresses, combined with the corresponding differential displacements. It is worth considering the inverse problem as well, and pin down the essential measurements needed during a monitoring campaign to infer the surface imperfection and consequently update any FE model of the designed connection. It is important to highlight that current standards do not provide allowable geometric tolerances for slip joints, which calls for a systematic sensitivity analysis concerning possible imperfections and their consequence on the slip joint's mechanical behaviour.

Concerning the design procedure, at the moment it mainly relies on meeting the minimum overlap length, standardized at 1.5 times the diameter of the used cones. A conservative approach concerning the impact of the imperfection is also taken, by assuming the worst case scenario during the overlap of the two cones: either a narrow contact area is formed at the bottom or at the top of the slip joint. However, current guidelines lack in providing manufacture tolerances for the slip joint, also because the knowledge on the impact of cone imperfections on the slip joint assembly is still at a rudimentary stage. In the specific case investigated in this study, cone imperfections did not prevent to meet the design overlap (5.20 m), and it did not affect the global behaviour of the wind turbine structure. The latter was confirmed by comparing the modal analysis result of a FE model (based on full bonded condition between the two connecting parts) with the first natural frequency of the wind turbine structure observed from experimental data, as shown in [34] and also in Fig. 8. However, as shown throughout the paper, cone imperfections do influence the local stresses of the slip joint. Besides the improvements of the FE model suggested above, the authors would propose conducting more laboratory tests to better capture the mechanical behaviour of the slip joint under different loading conditions, in order to better understand the behaviour of the two connecting parts. In addition to the impact of imperfections on the local stresses, the slip joint relies on the friction force developed between the two contacting coated surfaces, for which not much knowledge is available in the published literature.

As a final remark concerning eventual questions from the readers' side, the first author is available to provide information concerning the modelling part, while the second author is informed about the experimental part and further research lines concerning the slip joint.

6.2. Conclusions

The aim of this study is illustrate a first view of the available data collected from a unique monitoring campaign for a slip joint connection of an offshore wind turbine. The contribution focuses on the most relevant loading events, and made a first attempt to capture the qualitative

behaviour of axial and hoop stresses through an ideal and simplified Finite Element model of the slip joint. While the behaviour of the axial stresses could be fairly matched by an ideal Finite Element model, the behaviour of the hoop stresses indicated the need of including surface imperfections in the numerical model. Besides the relevance of the manufacturing imperfections, a correct modelling approach has to account for the induced prestress present in the slip joint and caused by settlements due to the loading history. A first form of prestress is provided by the initial installation process, while second order terms of prestress are due to loading events that lead to residual displacements leaving the slip joint in a temporary "stick" condition. Besides few modelling discrepancies, the slip joint behaviour observed thanks to the experimental data, proved to be rather consistent throughout the monitoring campaign, characterized by diversified loading events. This suggests that a more refined model, based on the actual knowledge of the surface imperfections and its frictional behaviour, would be sufficient to effectively design a slip joint, and predict its mechanical behaviour in long term.

CRediT authorship contribution statement

Maroš Mojto: Writing – review & editing, Writing – original draft, Visualization, Validation, Investigation, Formal analysis, Data curation. **Alessandro Cabboi:** Writing – review & editing, Writing – original draft, Supervision, Methodology, Investigation, Conceptualization.

Declaration of competing interest

The authors declare the following financial interests/personal relationships which may be considered as potential competing interests: Alessandro Cabboi reports financial support was provided by Netherlands Enterprise Agency.

Data availability

Data will be made available on request.

Acknowledgements

The work was part of the Slip Joint Offshore Research project (ref. TEHE116334-SJOR) and of the Slip Joint Offshore Qualification project (ref. TEHE117056-SJOQ), partially funded by the Dutch government. The authors would like to thank two industrial partners of both projects, VanOord (Suur Sander) and DOT (Thijs Kamphuis), for the constructive discussions during the projects and for sharing the experimental data.

References

[1] E. de Vries, Offshore monopile failure - a solution may be in sight, wind power monthly magazine, 2010, URL https://www.windpowermonthly.com/article/1011507.
[2] NoordzeeWind, Operations report 2009, Technical Report, NoordzeeWind, 2009, URL http://www.noordzeewind.nl/wp-content/uploads/2012/02/OWEZ_R_000_20101112_Operations_2009.pdf.
[3] DNV, Joint industry project summary report from the JIP on the capacity of the grouted connections in offshore wind turbine structures, Technical Report 2010–1053, Det Norske Veritas AS, 2011a.
[4] P. Dallyn, A. El-Hamalawi, A. Palmeri, R. Knight, Experimental testing of grouted connections for offshore substructures: A critical review, Structures 3 (2015) 90–108.
[5] P. Dallyn, A. El-Hamalawi, A. Palmeri, R. Knight, Experimental investigation on the development of wear in grouted connections for offshore wind turbine generators, Eng. Struct. 113 (2016) 89–102.
[6] N.I. Tziavos, H. Hemida, N. Metje, C. Baniotopoulos, Grouted connections on offshore wind turbines: a review, Proc. Inst. Civ. Eng. - Eng. Comput. Mech. 169 (4) (2016) 183–195.
[7] J.-H. Lee, D.-H. Won, Y.-J. Jeong, S.-H. Kim, Y.-J. Kang, Interfacial shear behavior of a high-strength pile to sleeve grouted connection, Eng. Struct. 151 (2017) 704–723.
[8] P. Schaumann, A. Raba, A. Bechtel, Fatigue behaviour of grouted connections at different ambient conditions and loading scenarios, in: Energy Procedia, 14th Deep Sea Offshore Wind R&D Conference, EERA DeepWind 2017, Vol. 137, 2017, pp. 196–203.
[9] T. Chen, Z. Xia, X. Wang, Q. Zhao, G. Yuan, J. Liu, Experimental study on grouted connections under static lateral loading with various axial load ratios, Eng. Struct. 176 (2018) 801–811.
[10] J. Henneberg, P. Schaumann, Numerical analysis of early age movement in grouted connections, in: ce/papers - Proceedings in Civil Engineering, 9th International Conference on Composite Construction in Steel and Concrete, Stromberg, Germany, July 26-30, 2021, Vol. 6, (1) 2023, pp. 289–301.
[11] I. Lotsberg, A. Serednicki, A. Lervik, H. Bertnes, Design of grouted connections for monopile offshore structures, Stahlbau 81 (9) (2012) 695–704.
[12] M. Voßbeck, T. Löhning, M. Kelm, Structural behaviour of grouted connections for monopile foundations of offshore wind turbines, Stahlbau 82 (1) (2013) 55–60.
[13] I. Lotsberg, Structural mechanics for design of grouted connections in monopile wind turbine structures, Mar. Struct. 32 (2013) 113–135.
[14] W. Njomo-Wandji, A. Natarajan, N. Dimitrov, Probabilistic structural assessment of conical grouted joint using numerical modelling, Ocean Eng. 158 (2018) 232–252.
[15] T. Chen, X. Wang, G. Yuan, J. Liu, Fatigue bending test on grouted connections for monopile offshore wind turbines, Mar. Struct. 60 (2018) 52–71.
[16] N. Tziavos, H. Hemida, N. Metje, C. Baniotopoulos, Non-linear finite element analysis of grouted connections for offshore monopile wind turbines, Ocean Eng. 171 (2019) 633–645.
[17] P. Schaumann, M. Böhm, K. Schürmann, Improvements in the fatigue design of support structures for offshore wind turbines, Steel Constr. 14 (2) (2021) 74–82.
[18] K.S. Jensen, S.J. Petersen, R.R. Pedersen, European offshore wind engineering - past, present and future, Proc. Inst. Civ. Eng.: Civ. Eng. 171 (4) (2018) 159–165.
[19] S. Chaki, G. Cornelup, I. Lillamand, H. Walaszek, Combination of longitudinal and transverse ultrasonic waves for in situ control of the tightening of bolts, J. Press. Vessel Technol. 129 (2006) 383–390.
[20] S.M. Sah, J.J. Thomsen, M. Brøns, A. Fidlin, D. Tcherniak, Estimating bolt tightness using transverse natural frequencies, J. Sound. Vib. 431 (2018) 137–149.
[21] SHK, Olycka med vindkraftverk i Lemnhult, Vetlanda kommun, Jönköpings län, den 24 december 2015, Technical Report RO 2017:01, Swedish Accident Investigation Authority, 2017.
[22] K.E.Y. Creusen, G. Misios, J.S. Winkes, M. Veljkovic, Introducing the C1 wedge connection, Steel Constr. 15 (1) (2022) 13–25.
[23] B. Lutje Schipholt, J. Van Der Tempel, The slip-joint connection - alternative connection between pile and tower, Technical Report, DOWEC, 2003.
[24] SJOR – slip joint offshore research project, 2016-2019, URL https://grow-offshorewind.nl/project/sjor.
[25] S. Suur, F. Hengeveld, Borssele v slip joint connection: design, certification and installation of the world's first full-size submerged slip joint, Steel Constr. 15 (3) (2022) 152–159.
[26] R. Slocum, M. Fairbairn, Slip joints connections: How do these things work? in: Electrical Transmission and Substation Structures 2015, ASME, 2015, pp. 363–374.
[27] International Electrotechnical Commission, Overhead electrical lines exceeding AC 45 kV. Part 1: General requirements. Common specifications, chapter 7.4.6.3, 2001, EN 50341-1:2012.
[28] M. Botló, M. Magura, J. Brodniansky, J. Brodniansky, Numerical and experimental analysis of structural details of electrical transmission line towers, in: Proceedings of IASS Annual Symposia, IASS 2016 Tokyo Symposium: Spatial Structures in the 21st Century – General: Towers & Temporary Structures - Preservation, (1) 2016, pp. 1–8.
[29] J. Brodniansky, T. Klas, J. Brodniansky, M. Magura, J. Recký, M. Tilinger, Field tests, laboratory evaluation and modelling of slip joints, in: Proceedings of IASS Annual Symposia, IASS 2019 Barcelona Symposium: Computational Methods, (18) 2019, pp. 1–8.
[30] J. Brodniansky, J. Recký, M. Magura, T. Klas, M. Botló, Advances and Trends in Engineering Sciences and Technologies III, CRC Press, 2019, pp. 55–60, chap. Slip joint connection of conical towers subjected to bending and torsion.
[31] M. Mojto, J. Brodnianský, J. Brodnianský, J. Recký, M. Tilinger, Modelling and experimental tests of spatial structure focused on slip joints, in: Proceedings of IASS Annual Symposia, IASS 2020 Surrey Symposium: Metal gridshell structures, connections, and stability, (18) 2020, pp. 1–9.
[32] M. Mojto, J. Brodnianský, B. Ján, The effect of manufacturing imperfections in the slip joints, IOP Conf. Ser.: Mater. Sci. Eng. 1252 (1) (2022) 012026, http://dx.doi.org/10.1088/1757-899X/1252/1/012026.
[33] A. Cabboi, M. Segeren, H. Hendrikse, A. Metrikine, Vibration-assisted installation and decommissioning of a slip-joint, Eng. Struct. 209 (2020).
[34] A. Cabboi, T. Kamphuis, E. van Veldhuizen, M. Segeren, H. Hendrikse, Vibration-assisted decommissioning of a slip joint: Application to an offshore wind turbine, Mar. Struct. 76 (2021).
[35] SJOQ – slip joint offshore qualification project, 2018-2019, URL https://projecten.topsectorenergie.nl/projecten/slip-joint-offshore-qualification-31377.
[36] T. Kamphuis, Design, testing and verification of the DOT500 slip joint support structure, (Master thesis), Delft University of Technology, 2016, URL http://resolver.tudelft.nl/uuid:22375c41-8627-4509-bf94-5da3559d1002.
[37] Ansys, 2020, Version 2020, https://www.ansys.com/.